Electronic Supplementary Material (ESI) for Journal of Materials Chemistry A.

Supplementary Information

A predictive model of surface adsorption in dissolution on transition metals and alloys

Bo Li, Xin Li, and Wang Gao*

Key Laboratory of Automobile Materials, Ministry of Education, Department of Materials Science and Engineering, Jilin University 130022, Changchun, China

Table of Contents **Page**

Note S1: Details of the adsorption process in dissolution.

The adsorption process in dissolution contains several steps, which are shown in Fig. S2 for transition metal (TM) (111) surface. The adsorption order in dissolution is denoted by the symbol Ⓩ. Taking the (2 × 2) supercell for an example, the symbol ① denotes the adsorption on the undissolved surfaces, while the symbols ②, ③, and ④ denote the adsorption on the surfaces with one, two, and three atoms dissolved respectively. Similarly, the symbols ①-⑨ denote the corresponding adsorption order as the dissolution proceeds for the (3 × 3) supercell. For near-surface alloys (NSAs), the dissolution process is the same as that for TMs since the surface of NSAs consists of only one element (Fig. S3a-d). For binary alloys (BAs), the practical dissolution order is adopted, namely, the dissolution proceeds along the line composed of the same element shown in Fig. S3e-h. For high-entropy alloys (HEAs), the similar steps as TMs are adopted for simulating the surface adsorption in dissolution, which don't correspond to the practical dissolution order of the different components (Fig. S4). Nevertheless, our calculations for HEAs are representative enough by studying the adsorption-site effect of alloying, the environmental effect of alloying, and the coupling of them, which consider all the possible cases of adsorption in dissolution (including the practical dissolution order).

It is noteworthy that the adsorption-site and environmental effects of alloying in our study don't break the periodic structure of NSAs and BAs. On NSAs and BAs, the adsorption-site effect of alloying denotes the change of the chemical composition of the adsorption site and the surrounding atoms that are the same as the adsorption site, while the environmental effect of alloying does the change of the chemical properties of the surrounding atoms that are different from the adsorption site. On HEAs, the adsorption-site effect of alloying denotes the change of the chemical composition of adsorption sites but fixing the surrounding environment, whereas the environmental effect of alloying does the change of the surrounding environment but fixing the adsorption sites. We also find that the adsorption energy on HEAs in the adsorption-site effect of alloying by changing only the element of adsorption sites or changing all the element that is the same as the adsorption site follows the same linear relation (see Fig. S17a and b).

Note S2: The origin of the prefactors μ_1 and μ_2 of Eq. (3) in the main text and the essence of the cohesive energy descriptor.

Eq. (3) in the main text indicates that the prefactors μ_1 and μ_2 are determined by the valence of adsorbates, which can be deduced and rationalized from effective medium theory (EMT) and bond-order conservation criterion[1]. In EMT, the inhomogeneous environment of the host is replaced by the homogeneous electron gas, thereby simplifying the calculations of the energies of the adsorption system[2]. It has been demonstrated that the first-order approximation of EMT is essential for describing the adsorption of atoms that are not particularly polarizable such as hydrogen and oxygen[2]. Note that the zero-order approximation of EMT has been derived by Nørskov *et al*[3] with the relation $E^{(0)} \propto \frac{(X_\mathrm{m} - X)n_0}{X_\mathrm{m}}$ (n_0 is the homogeneous electron density). For the first-order approximation, we adopt a simple perturbation effect induced by the adsorbed atom to the electron density as $\Delta n = \frac{n_0}{X_\mathrm{m}+1}$ ("1" stems from that the change of the bond number of an adsorbate upon adsorption is most likely an integer and one). By substituting n_0 with Δn in the zero-order term, the first-order term of EMT obeys that:

$$E^{(1)} \propto \frac{(X_\mathrm{m} - X)n_0}{X_\mathrm{m}(X_\mathrm{m}+1)} = (X_\mathrm{m} - X)n_0\left(\frac{1}{X_\mathrm{m}} - \frac{1}{X_\mathrm{m}+1}\right) \tag{S1}$$

Combining the zero-order and the first-order terms of EMT, the adsorption energy of adsorbates that are not particularly polarizable obeys the relation as,

$$E_\mathrm{ad} = E^{(0)} - E^{(1)} \propto \frac{(X_\mathrm{m} - X)n_0}{X_\mathrm{m}+1} \tag{S2}$$

This exactly corresponds to the prefactor μ_1 of Eq. (3) in the main text. The prefactor μ_2 of Eq. (3) in the main text, $\frac{X+1}{X_\mathrm{m}+1}$, can be rationalized by the bond-order conservation criterion. The adsorption energy is proportional to the coordination number of surface sites, namely the saturated-bond number of surface sites. This relation should also hold from the point of view of adsorbates. Thus, the adsorption energy is proportional to the bond number of adsorbates, corresponding to the prefactor $\frac{X+1}{X_\mathrm{m}+1}$.

Tables S1, S2, S4 and S5 show that the DFT-calculated prefactors μ_1 and μ_2 for the adsorption energy on TMs, NSAs, BAs, and HEAs are in good agreement with the predictions by Eq. (3) in the main text. This demonstrates that the EMT and bond-order conservation criterion are general in describing the adsorption on TMs and alloys.

Note that the prefactors μ_1 and μ_2 of Eq. (3) in the main text are suitable for the adsorbates with one kind of functional group binding to the central atom. For the adsorbates with two kinds of functional groups binding to the central atom such as COOH, CHO, and CHOH, the prefactors μ_1 and μ_2 are $\mu_1 = 1/10 \times [(X_\mathrm{m} - X)/(X_\mathrm{m}+1) - X'/(X'_\mathrm{m}+1)]$ and $\mu_2 = 1/5 \times [(X+1)/(X_\mathrm{m}+1) + X'/(X'_\mathrm{m}+1)]$, where X' and X'_m are the actual bonding number and the maximum bondable number of the central atom for the second functional group[1]. Accordingly, the prefactors μ_1 and μ_2 are $\mu_1 = 0.027$ and $\mu_2 = 0.147$ for COOH, $\mu_1 = 0.030$ and $\mu_2 = 0.140$ for CHO, and $\mu_1 = 0.047$ and $\mu_2 = 0.106$ for CHOH.

The cohesive energy E_coh of adsorption-site atoms depends on the *d*-band width and *s*-band depth[4]. E_coh can be separated into the *d*-band and *s*-band contributions with $E_\mathrm{coh} = E^\mathrm{d}_\mathrm{coh} + E^\mathrm{s}_\mathrm{coh}$. According to the tight-binding (TB) approximation[5–7], the *d*-band contribution to E_coh is calculated by the density of states of the *d* band as,

$$E^\mathrm{d}_\mathrm{coh} = \int_{B_\mathrm{d}}^{E_\mathrm{f}} (E_\mathrm{d} - E) n_\mathrm{d}(E) \mathrm{d}E \tag{S3}$$

where B_d and E_f are the *d*-band bottom and Fermi level, $n_\mathrm{d}(E)$ is the density of states of the *d* bands, and E_d is the energy of the atomic *d*-level spreading into a band of finite width W_d. The *s*-band contribution to E_coh can be estimated with the relation as[8],

$$E_{\mathrm{coh}}^{\mathrm{s}} = \int_0^{E_{\mathrm{f}}} E n_{\mathrm{s}}(E)\mathrm{d}E = \int_0^{E_{\mathrm{f}}} \frac{2}{3\pi}\left[\frac{2\pi E m_{\mathrm{e}} r_0^5}{\hbar^2(\pi r_0^3 + 5r_{\mathrm{d}}^3)}\right]^{3/2} \mathrm{d}E \quad \text{(S4)}$$

where $n_{\mathrm{s}}(E)$ is the density of electron states of the *s* bands. r_0 corresponds to the atomic radius that is related to the *s*-band depth, r_{d} is the *d*-state radius, m_{e} is the electron mass and h is the Plank constant. Combining Eqs. (S3) and (S4), one can obtain that the cohesive energy depends on the *d*-band width and *s*-band depth. In particular, the *s*-band contribution to the cohesive energy varies significantly from one metal to the next (*s*-band contribution to the cohesive energy is about 2.44~6.08 eV, accounting for 38%~100% of the total cohesive energy)[4]. Therefore, the *s*-band contribution plays an important role in the cohesive energy.

Note S3: The environmental effect of alloying on the adsorption energy and the adsorption at the different sites of TMs and alloys.

Fig. 2c and d in the main text and Fig. S22 demonstrate that the adsorption energy of CH_x (x=0-3), NH_x (x=0-2), CO, OH, F, and Cl on Pt(Pd)M NSAs, AgM BAs, and Ru(Cu)RhIrPdPt HEAs in the environmental effect of alloying (namely fixing the chemical composition of adsorption sites and altering the surrounding environment) also follows the linear relations in the adsorption-site effect of alloying. Since k_1 and k_2 reflect the electronic localization of alloys in adsorption, one can estimate the electronic localization of the different alloying elements in determining the adsorption energy according to the ratio of these two prefactors. For the CH_2 adsorption on HEAs, the ratio k_1/k_2 is 0.67 for dissolving Ru element, 0.80 for dissolving Ir element, 0.91 for dissolving Pt element, 2.65 for dissolving Pd element, and 12.17 for dissolving Rh element (see Table S3). Therefore, the electronic localization of alloying elements in RuRhIrPdPt HEAs in adsorbing CH_2 during the dissolution obeys the order of Ru > Ir > Pt > Pd > Rh. Similarly, Cu is more local than Ru in adsorbing CO on Ru(Cu)RhIrPdPt HEAs (see Table S3).

In this study, we have considered the adsorption energy of various adsorbates at the top, bridge, fcc, hcp, and four-fold sites of (100), (110), (111), and (211) surfaces of TMs, the top and fcc sites of (100) and (111) surfaces of NSAs, the top, bridge, fcc, hcp and four-fold sites of (100), (111) and (211) surfaces of BAs, and the top and bridge sites of (100), (110), (111), (211) and (532) surfaces of HEAs. Encouragingly, all these adsorption energies at the various sites of TMs and alloys can be well described by the electronic and geometric descriptors D_{ad} and $\overline{CN}$, which demonstrates the universality of our scheme (see Fig. 2 in the main text and Figs. S13-S15, S20-S24)[9-18]. It is noteworthy that for the OH adsorption at the bridge sites of HEAs, the prefactor μ_1 fulfills the prediction by Eq. (3) in the main text, while the prefactor μ_2 [$\mu_2 = 3/5\times(X+1)/(X_m+1)$] is three times of that at the top site [$\mu_2 = 1/5\times(X+1)/(X_m+1)$] (see Fig. 2f in the main text). This indicates that the contribution of geometric effect to the OH adsorption energy at the bridge sites of HEAs is greater than that at the top site.

Note S4: The reaction energy, activation energy, and catalytic activity on TMs and alloys.

To identify the accuracy of our scheme in predicting the reactivity at surfaces, we revisit several widely-studied reactions on TMs and alloys, including the decomposition of CH_4, NH_3, N_2 and H_2O, thermochemical formation of H_2O and H_2, decolorization reaction, CO_2 reduction reaction (CO_2RR), hydrogen evolution reaction (HER), oxygen reduction reaction (ORR), and oxygen evolution reaction (OER). We have studied the reaction energy of 23 different reaction pathways including $CO_2 + H^+ + e^- \rightarrow COOH^*$, $COOH^* + H^+ + e^- \rightarrow CO^* + H_2O$, $CO^* + H^+ + e^- \rightarrow COH^*$, $CO^* + H^+ + e^- \rightarrow CHO^*$, $COH^* + H^+ + e^- \rightarrow C^* + H_2O$, $C^* + H^+ + e^- \rightarrow CH^*$, $CH^* + H^+ + e^- \rightarrow CH_2^*$, $CH_2^* + H^+ + e^- \rightarrow CH_3^*$, $CH_3^* + H^+ + e^- \rightarrow CH_4$, $COH^* + H^+ + e^- \rightarrow CHOH^*$, $CHOH^* + H^+ + e^- \rightarrow CH_2OH^*$, $CH_2OH^* + H^+ + e^- \rightarrow CH_3OH$, $CH_4 \rightarrow CH_3^* + H^*$, $CH_3^* \rightarrow CH_2^* + H^*$, $CH_2^* \rightarrow CH^* + H^*$, $CH^* \rightarrow C^* + H^*$, $NH_3^* \rightarrow NH_2^* + H^*$, $NH_2^* \rightarrow NH^* + H^*$, $NH^* \rightarrow N^* + H^*$, $N_2 \rightarrow 2N^*$, $H_2O \rightarrow OH^* + H^*$, $OH^* \rightarrow O^* + H^*$ and $OH^* + H^* \rightarrow H_2O$ on TMs, NSAs, and BAs (Figs. S27-S29 and S34)[13,14,18-25], the activation energy of 13 different reaction pathways including $CO^* + H^+ + e^- \rightarrow CHO^*$, $CH_4 \rightarrow CH_3^* + H^*$, $CH_3^* \rightarrow CH_2^* + H^*$, $CH_2^* \rightarrow CH^* + H^*$, $CH^* \rightarrow C^* + H^*$, $NH_3^* \rightarrow NH_2^* + H^*$, $NH_2^* \rightarrow NH^* + H^*$, $NH^* \rightarrow N^* + H^*$, $N_2 \rightarrow 2N^*$, $H_2O \rightarrow OH^* + H^*$, $OH^* \rightarrow O^* + H^*$, $OH^* + H^* \rightarrow H_2O$, and $2H^* \rightarrow H_2$ on TMs, NSAs and HEAs (Figs. S31, S32, S35 and S37)[13,14,19,21-24,26-29], and the experimental- and theoretical-estimated catalytic activity (current density, onset potential, conversion efficiency, decoloration time, overpotential, Tafel slope and turnover frequency) of decolorization reaction, CO_2RR, HER, ORR, OER, and NH_3 decomposition on TMs, NSAs, BAs, and HEAs (Figs. S33, S36, S40 and S41)[30–39]. The symbol * indicates the adsorption state, while H^+ denotes a proton from electrolytes.

The reaction energy (E_r) of a heterogeneous catalytic reaction corresponds to the adsorption-energy difference between a reactant and a product. One thus can calculate the reaction energy on TMs and alloys based on our model Eqs. (3-5) in the main text. For electrochemical reactions, such as the protonation of hydrocarbons $CH_{x1}^* + (x_2 - x_1)H^+ + (x_2 - x_1)e^- \rightarrow CH_{x2}^*$, the reaction energy is determined by the adsorption-energy difference between CH_{x1}^* and CH_{x2}^* and the contribution of H^+ to the reaction energy is constant, from one catalyst to another. According to Eq. (3) in the main text, the reaction energy of an electrochemical reaction step for a reactant and a product with the same central atom obeys the relation as,

$$E_r = \lambda_{r1} D_{ad} + \lambda_{r2} \overline{CN} + \theta_{1,2} = \frac{1}{10} \times \frac{X_1 - X_2}{X_m + 1} D_{ad} - \frac{1}{5} \times \frac{X_1 - X_2}{X_m + 1} \overline{CN} + \theta_{1,2} \quad \text{(S5)}$$

X_1 and X_2 are the actual bonding number for the reactant and product. Eq. (S5) can describe well the available electrochemical reaction energies, such as those of CO_2RR on TMs (see Fig. S27), with the predicted prefactors λ_{r1} and λ_{r2} in good agreement with the fitted values for all available 12 different reaction steps (see Table S7). For thermochemical reactions, the interaction between the species in reactants or products is also crucial to the reaction energy. Taking the decomposition of hydrocarbons [$CH_{x1}^* \rightarrow CH_{x2}^* + (x_1 - x_2)H^*$] as an example, the contribution of H^* (including the adsorption of H^* and the interactions between H^* and CH_{x2}^*) is also indispensable to the trend of reaction energies on different substrates. Thus the reaction energy should follow the relation of $\Delta E \propto [1/10 \times (X_1 - X_2)/(X_m + 1) + \mu_{1,H^*}] D_{ad} + [-1/5 \times (X_1 - X_2)/(X_m + 1) + \mu_{2,H^*}] \overline{CN}$. By analyzing a large number of reaction energies of 5 different reactions (including the decomposition of CH_4, NH_3, N_2, and H_2O, and the formation of H_2O), we find that the prefactors μ_{1,H^*} and μ_{2,H^*} can approximately be expressed as $\mu_{1,H^*} = 1/20 \times (X_1 - X_2)/(X_m + 1)$ and $\mu_{2,H^*} = -1/10 \times (X_1 - X_2)/(X_m + 1)$. Accordingly, the reaction energy of the thermochemical reactions obeys the relation as,

$$E_r = \lambda_{r1} D_{ad} + \lambda_{r2} \overline{CN} + \theta'_{1,2} = \frac{3}{20} \times \frac{X_1 - X_2}{X_m + 1} D_{ad} - \frac{3}{10} \times \frac{X_1 - X_2}{X_m + 1} \overline{CN} + \theta'_{1,2} \quad \text{(S6)}$$

Encouragingly, Eq. (S6) is effective in describing the reaction energy of all considered thermochemical reactions on TMs and alloys (see Figs.S28, S29, and S34), and the predicted prefactors λ_{r1} and λ_{r2} of Eq. (S6) are in agreement with the fitted values (see Table S7).

According to the Brønsted–Evans–Polanyi (BEP) relation[40], the activation energy (E_a) is linearly related to the reaction energy for surface reactions. By systematically studying the available activation energies of 7 different reactions on TMs and alloys (including CO_2RR, the decomposition of CH_4, NH_3, N_2 and H_2O, and the formation of H_2O and H_2), we find that the activation energy follows the relation of $E_a \propto (X_m + 2)/7E_r$ (see Fig. S30). Therefore, one can obtain that the activation energy obeys the relations as follows,

for electrochemical reactions,

$$E_a = \lambda_{a1} D_{ad} + \lambda_{a2} \overline{CN} + \beta_1 = \frac{1}{10} \times \frac{X_m + 2}{7} \times \frac{X_1 - X_2}{X_m + 1} D_{ad} - \frac{1}{5} \times \frac{X_m + 2}{7} \times \frac{X_1 - X_2}{X_m + 1} \overline{CN} + \beta_1 \quad \text{(S7)}$$

for thermochemical reactions,

$$E_a = \lambda_{a1} D_{ad} + \lambda_{a2} \overline{CN} + \beta_2 = \frac{3}{20} \times \frac{X_m + 2}{7} \times \frac{X_1 - X_2}{X_m + 1} D_{ad} - \frac{3}{10} \times \frac{X_m + 2}{7} \times \frac{X_1 - X_2}{X_m + 1} \overline{CN} + \beta_2, \quad \text{(S8)}$$

Eqs. (S7) and (S8) describe well the activation energies of all considered 7 different reactions on TMs and alloys (see Figs. S31, S32, and S35) and the predicted prefactors λ_{a1} and λ_{a2} of Eqs. (S7) and (S8) are also in agreement with the fitted values (see Table S8). Note that the correlation between the activation energy (reaction energy) and the electronic and geometric descriptors in Figs. S34a and S35d shows a v-shape behavior, which likely stems from the different structures of the CuNi NSAs. The available data in the left branch of the correlation belong to the CuNi NSAs with Ni alloying atoms in the topmost layer (CuNi-a ~ CuNi-f), while that in the right branch does the CuNi NSAs with Ni alloying atoms in the subsurface layer (CuNi-g). Notably, the negative and positive values of the slope likely depend on the contribution of the Pauli repulsion to the interactions between the metal *d* states and the adsorbate states[1,15]: if the Pauli repulsion contribution is dominant, the negative value; if the Pauli repulsion contribution is minor, the positive value. Moreover, Fig. S38 shows that HEAs can break the BEP relation (such as Fig. S38a and b), which is consistent with the findings by Rossmeisl et al[41]. This is likely due to that the reactants, transition states, and products interact with the surface atoms of HEAs with distinct electronic properties. Nevertheless, our descriptors can capture the trend of adsorption energies and activation energies on HEAs well (Figs. S37 and S39), since they depend on the specific active center and adsorption site. It is noteworthy that the activation energies in Fig. S37 contain the reactions with both changed and unchanged adsorption sites of reactants and products. For example, the blue line in Fig. S37a corresponds to the reactions with unchanged hcp adsorption sites of reactants and products, while the red line in Fig. S37a does the reactions with changed adsorption sites from the top and bridge sites of reactants to fcc sites of products and from the bridge and fcc sites of reactants to hcp sites of products. Therefore, our scheme is effective to capture the activation energies of reactions on HEAs no matter the adsorption sites from reactants to products change or not.

We also attempt to predict the reaction energies and activation energies by using Eqs. (S5-S8) as all parameters are easily accessible. The predicted MAE is about 0.19 eV for reaction energies and 0.16 eV for activation energies (see Fig. S42), both of which are smaller than the approximate error of (semi-)local functionals, ±0.2 eV. Moreover, our descriptors are also accurate in describing the trend of the theoretical and experimental reaction activities (see Figs. S33, S36, S40, and S41), where the fitted catalytic activity deviates less than 8%. All these results strongly support the effectiveness and reliability of our scheme in capturing the reactivity on TMs and alloys.

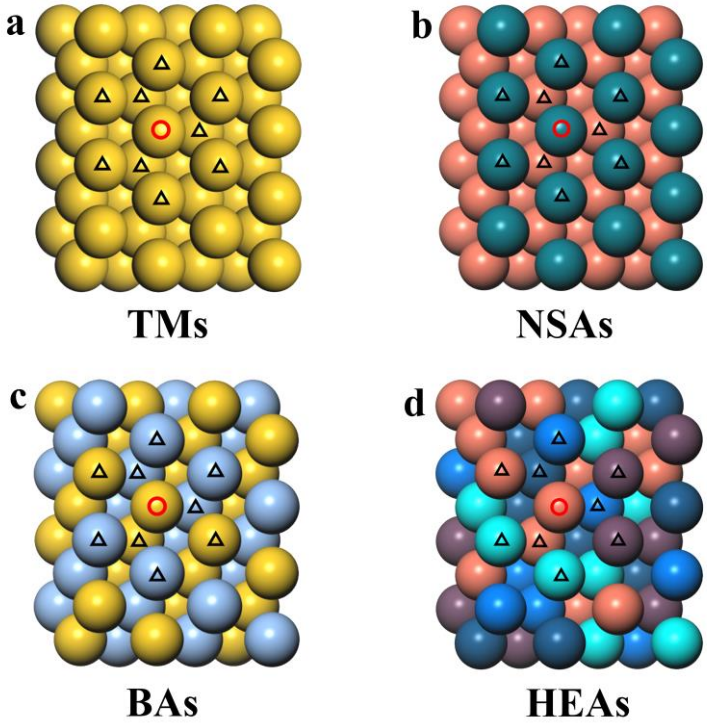

Figure S1. The atomic structures of (111) surface of TMs (a), NSAs with the topmost layer being the alloying element (b), BAs with the stoichiometric ratio of 1 between the two components (c), and HEAs (d). An active center on alloys for the top-site adsorption is plotted, which contains an adsorption site (the red circle) and its nearest neighbors (the black triangle). Note that the active center for the bridge- and hollow-site adsorption is defined in a similar way.

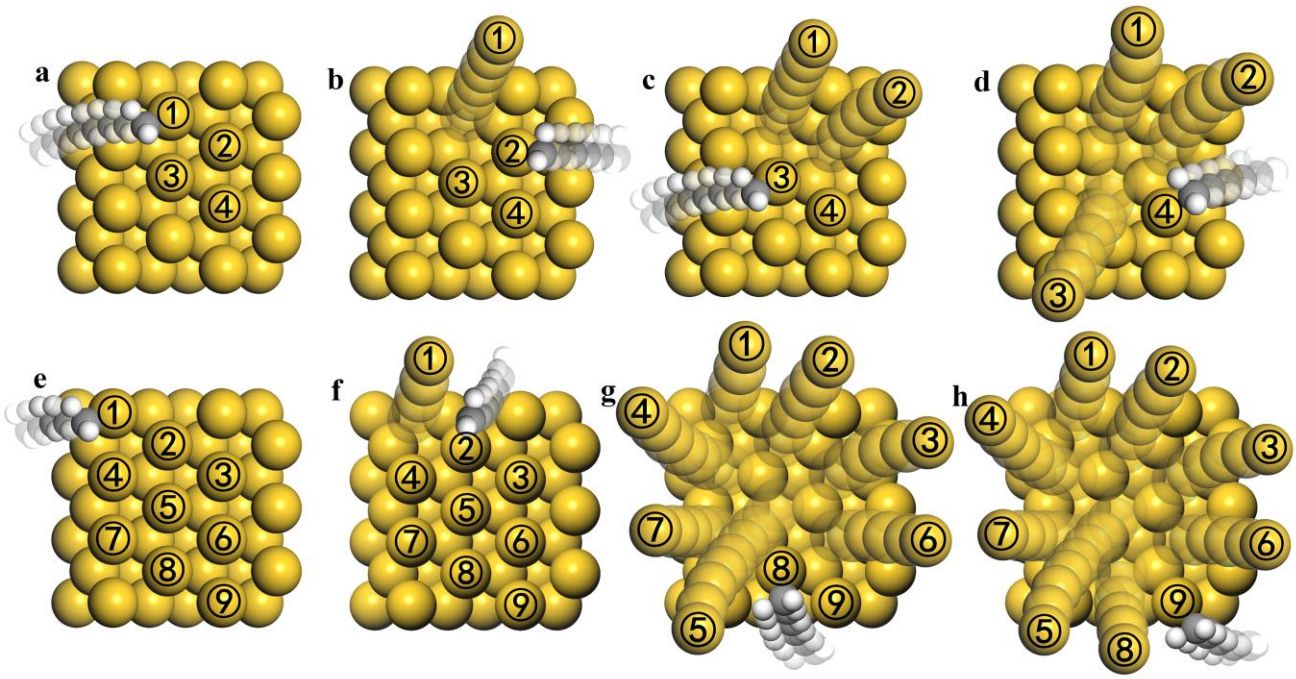

Figure S2. The schematic illustration of surface adsorption in dissolution on TMs with (2 × 2) and (3 × 3) supercells. The symbols ①-⑨ correspond to the dissolution order of surface atoms and the corresponding adsorption order as the dissolution proceeds. (a-d), (2 × 2) supercell. (e-h), (3 × 3) supercell.

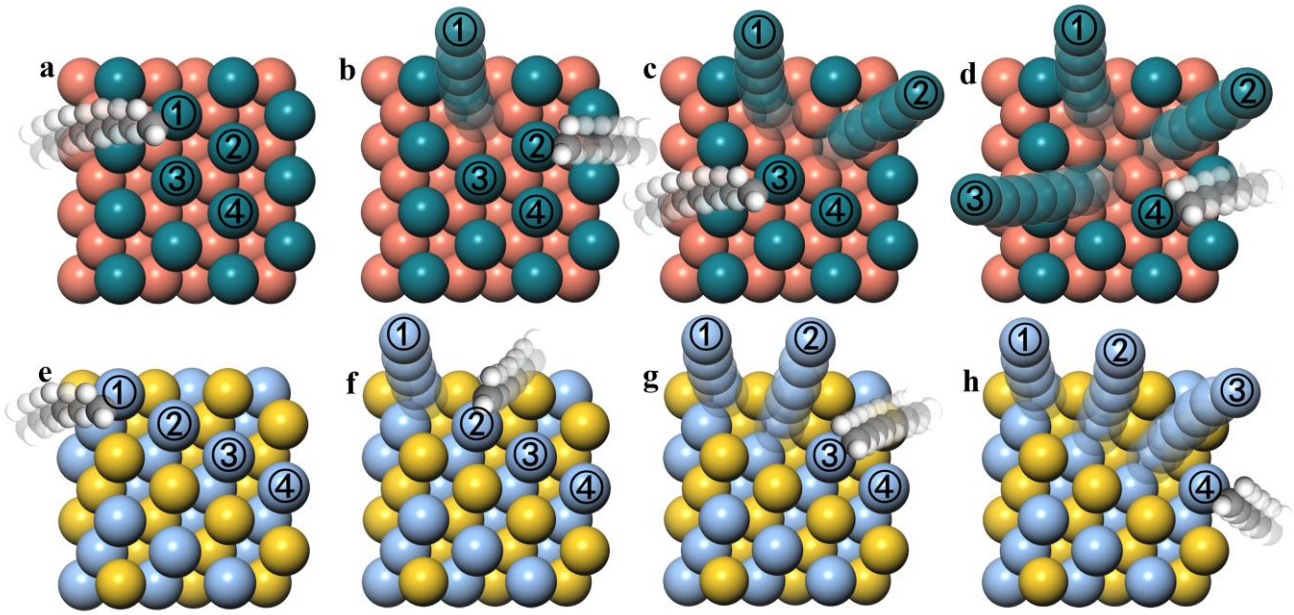

Figure S3. The schematic illustration of surface adsorption in dissolution on NSAs and BAs. The symbols ①-④ correspond to the dissolution order of surface atoms and the corresponding adsorption order as the dissolution proceeds. (a-d), NSAs. (e-h), BAs.

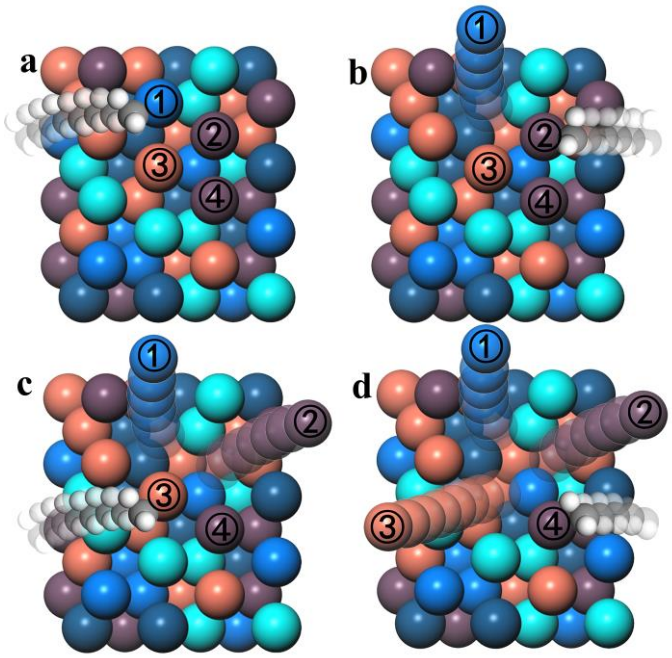

Figure S4. The schematic illustration of surface adsorption in dissolution on HEAs. The symbols ①-④ correspond to the dissolution order of surface atoms and the corresponding adsorption order as the dissolution proceeds.

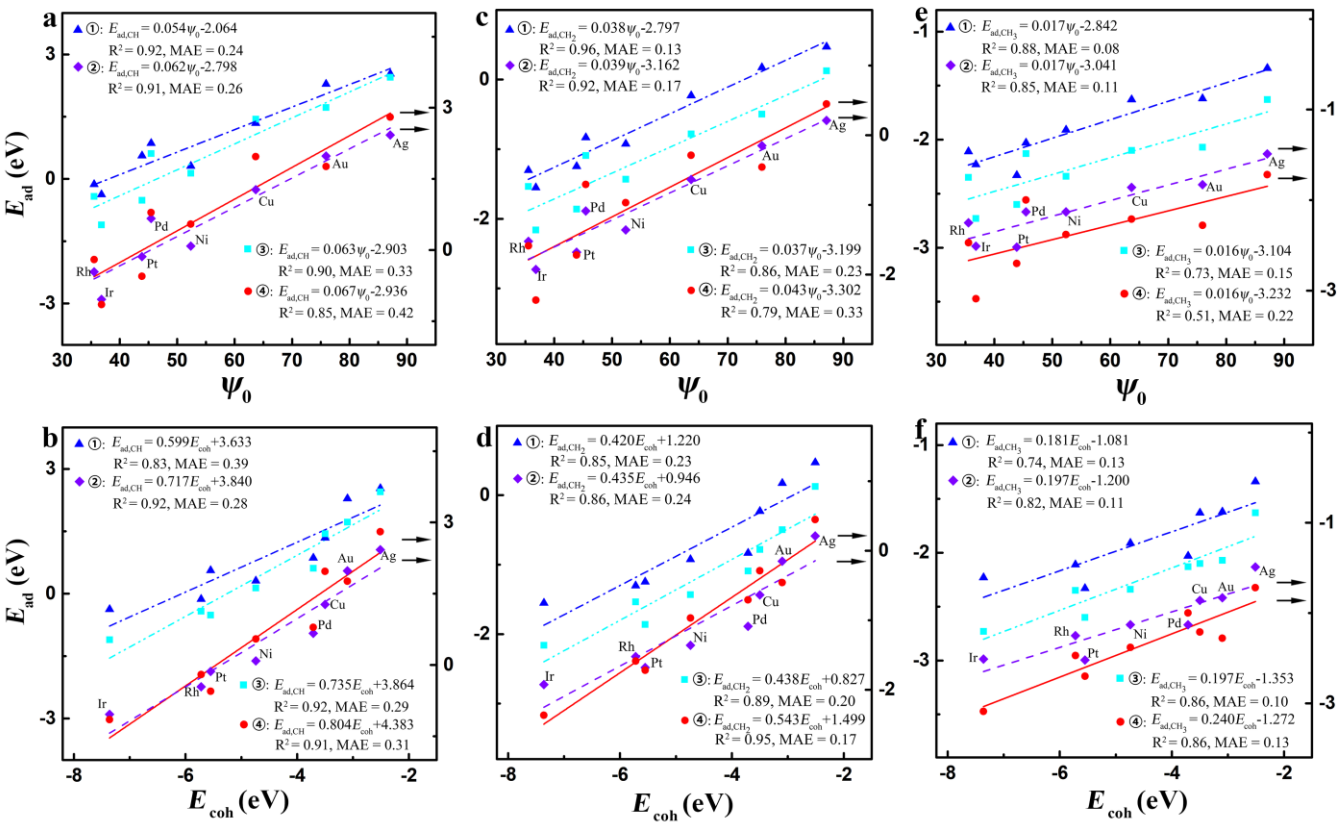

Figure S5. Comparison between the electronic descriptor ψ_0 and cohesive energy E_{coh} in describing the adsorption energy of CH, CH_2, and CH_3 on TM(111) surface in dissolution with (2 × 2) supercell. (a) and (b), CH. (c) and (d), CH_2. (e) and (f), CH_3[11]. Note that the data for CH and CH_2 adsorption are calculated by Perdew−Burke−Ernzerhof (PBE) functional[42] while those for CH_3 adsorption are calculated by revised PBE (RPBE)[43] functional.

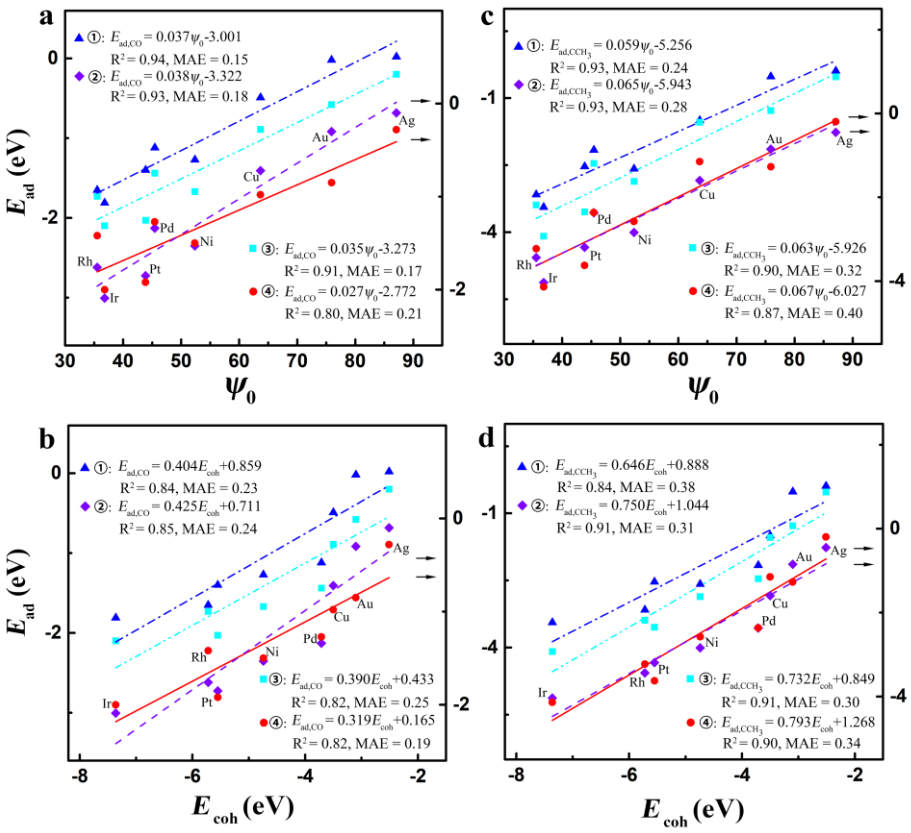

Figure S6. Comparison between the electronic descriptor ψ_0 and cohesive energy E_{coh} in describing the adsorption energy of CO and CCH_3 on TM(111) surface in dissolution with (2 × 2) supercell. (a) and (b), CO[11]. (c) and (d), CCH_3. Note that the data for CO adsorption are calculated by RPBE functional while those for CCH_3 adsorption are calculated by PBE functional.

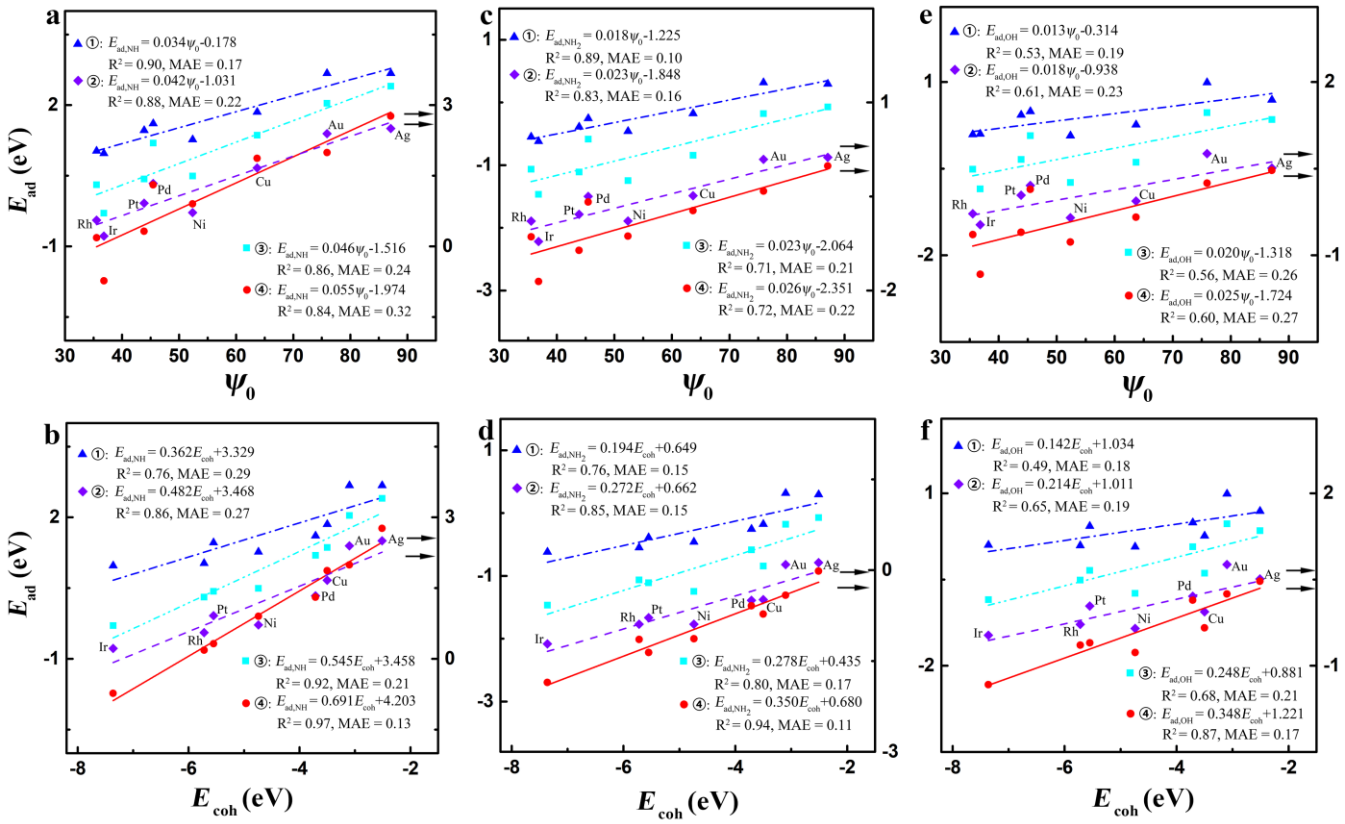

Figure S7. Comparison between the electronic descriptor ψ_0 and cohesive energy E_{coh} in describing the adsorption energy of NH, NH_2, and OH on TM(111) surface in dissolution with (2 × 2) supercell. (a) and (b), NH. (c) and (d), NH_2. (e) and (f), OH[11]. Note that the data for NH and NH_2 adsorption are calculated by PBE functional while those for OH adsorption are calculated by RPBE functional.

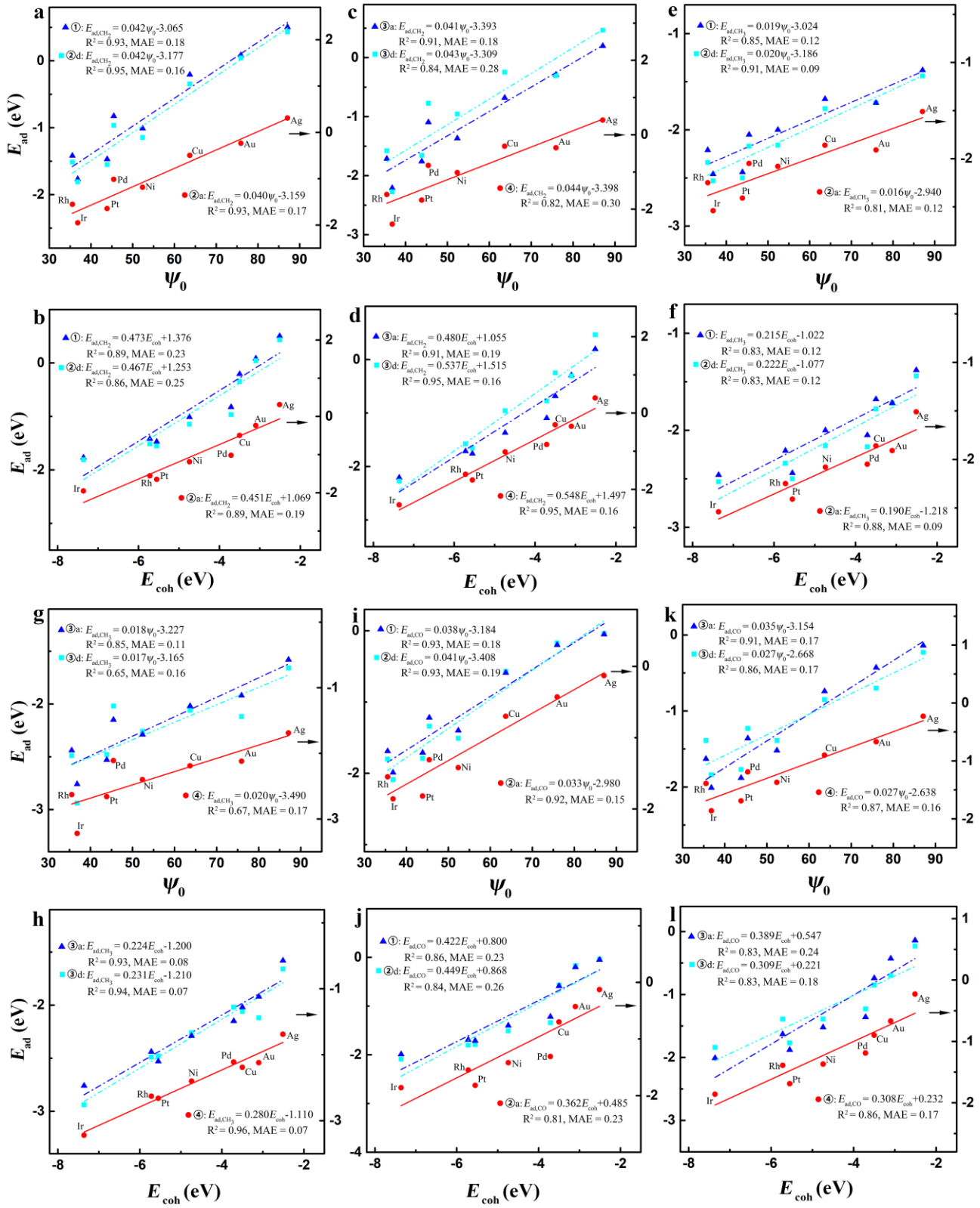

Figure S8. Comparison between the electronic descriptor ψ_0 and cohesive energy E_{coh} in describing the adsorption energy of CH_2, CH_3, and CO on TM(100) surface in dissolution with (2 × 2) supercell. (a-d), CH_2. (e-h), CH_3[11]. (i-l), CO[11]. Note that the data for CH_2 adsorption are calculated by PBE functional while those for CH_3 and CO adsorption are calculated by RPBE functional.

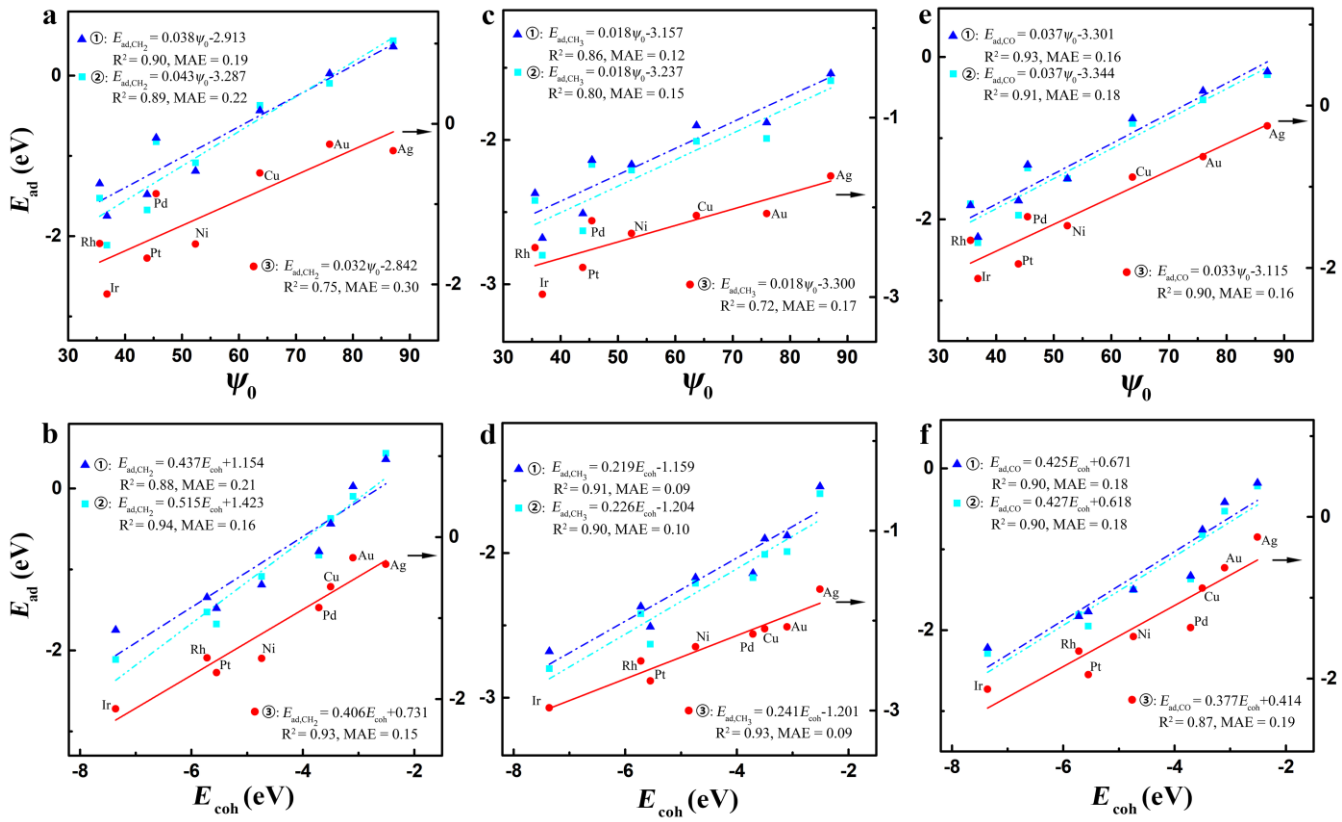

Figure S9. Comparison between the electronic descriptor ψ_0 and cohesive energy E_{coh} in describing the adsorption energy of CH_2, CH_3, and CO on TM(211) surface in dissolution with (1 × 3) supercell. (a) and (b), CH_2. (c) and (d), CH_3[11]. (e) and (f), CO[11]. Note that the data for CH_2 adsorption are calculated by PBE functional while those for CH_3 and CO adsorption are calculated by RPBE functional.

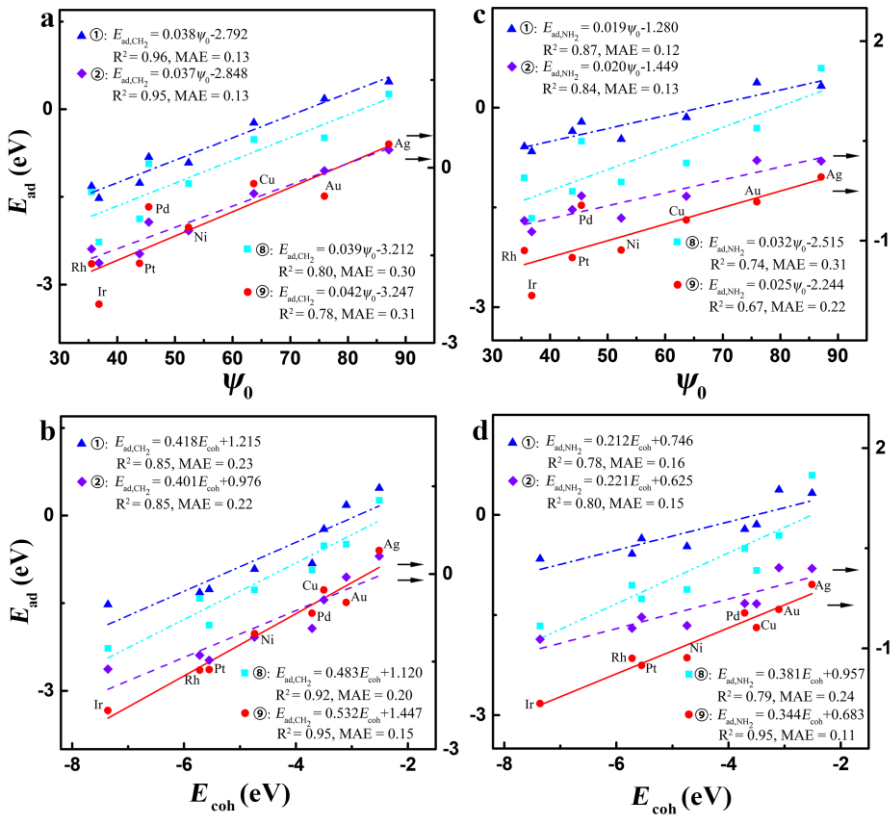

Figure S10. Comparison between the electronic descriptor ψ_0 and cohesive energy E_{coh} in describing the adsorption energy of CH_2 and NH_2 on TM(111) surface in dissolution with (3 × 3) supercell. (a) and (b), CH_2. (c) and (d), NH_2. All data are calculated with PBE functional.

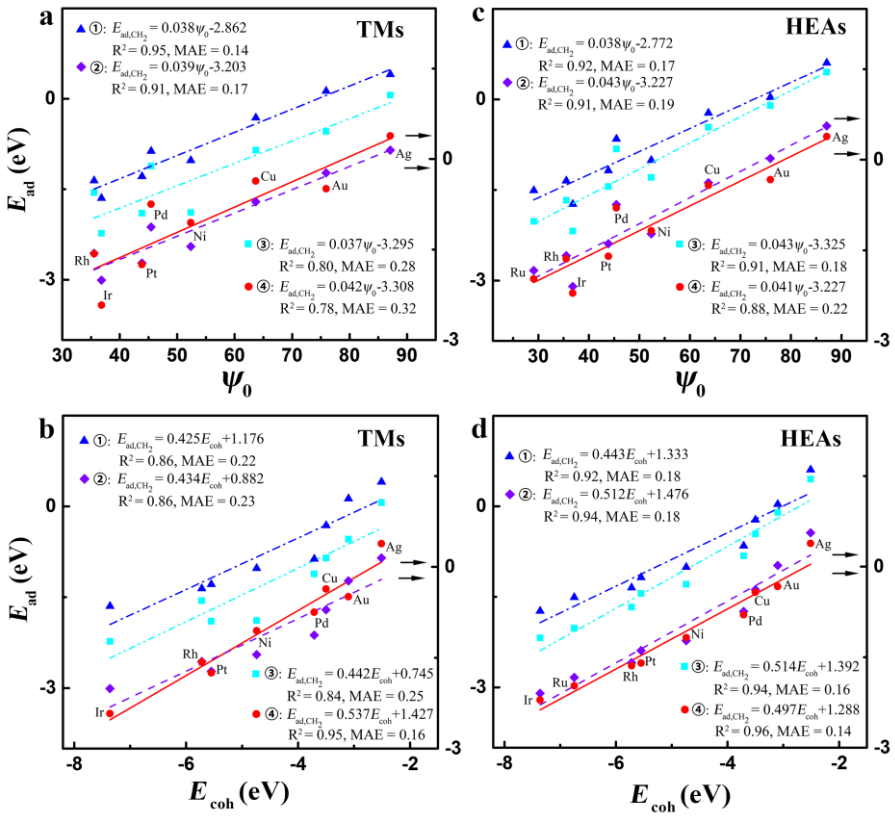

Figure S11. Comparison between the electronic descriptor ψ_0 and cohesive energy E_{coh} in describing the adsorption energy of CH_2 on (111) surface of TMs with (2 × 2) supercell and RuRhIrPdPt-based HEAs with (4 × 4) supercell in dissolution. (a) and (b), TMs. (c) and (d), HEAs. All data are calculated with Perdew-Wang-91 (PW91)[44] functional.

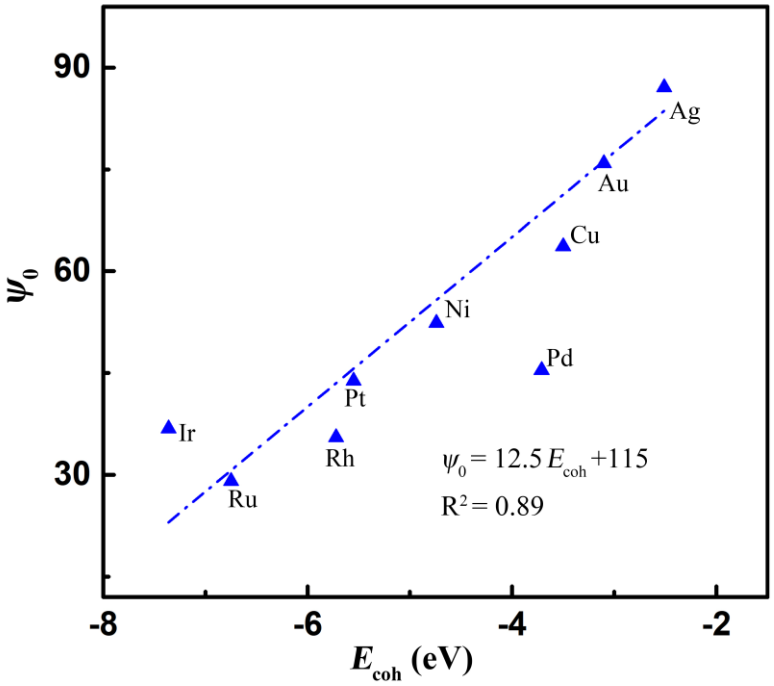

Figure S12. The correlation between the cohesive energy (E_{coh}) and the electronic descriptor ψ_0 on TMs[45]. Note that Pd is taken as an outlier in the linear fit.

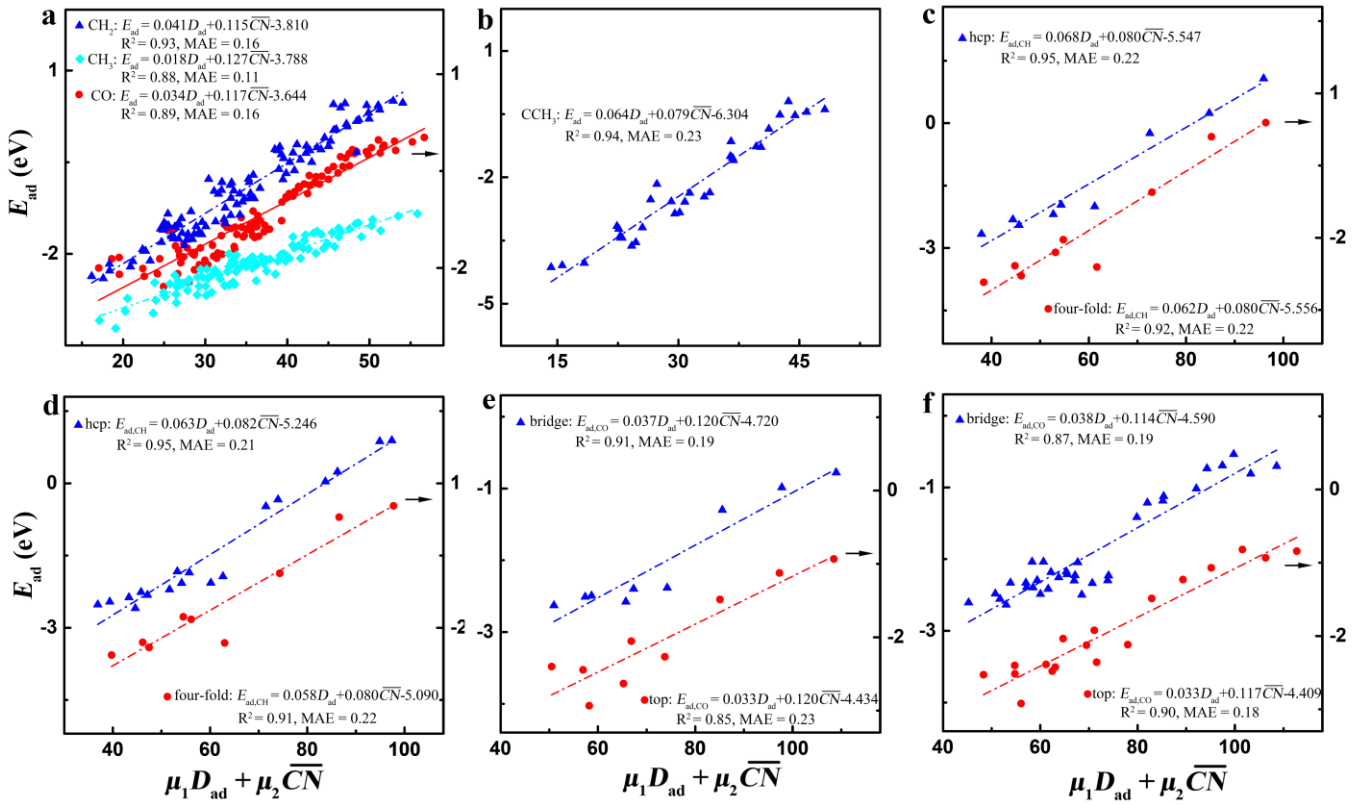

Figure S13. Adsorption energies of the different adsorbates against the electronic and geometric descriptors on TMs. (a), CH_2, CH_3[11], and CO[11] at the top site of (111), (100), and (211) surfaces in dissolution. Note that the data for CH_2 adsorption are calculated by PBE functional while those for CH_3 and CO adsorption are calculated by RPBE functional. (b), CCH_3 at the top site of (111) surface in dissolution obtained by PBE functional. (c), CH at the hcp site of the undissolved (111) surface and the four-fold site of the undissolved (100) surface[12]. (d), CH at the hcp and four-fold sites of the undissolved (211) surface[12]. (e), CO at the bridge site of the undissolved (100) surface and the top site of the undissolved (110) surface[12]. (f), CO at the bridge and top sites of the undissolved (211) surface[12]. The data in (c-f) are obtained by Bayesian error estimation functional with van der Waals correlation (BEEF-vdW)[46] functional. Note that the data in subfigures (a) and (b) are calculated with (2 × 2) supercell for (111) and (100) surfaces and (1 × 3) supercell for (211) surface, while those in subfigures (c)-(f) are calculated with (3 × 3) supercell for (111) and (100) surfaces, (2 × 3) supercell for (110) surface, and (1 × 3) supercell for (211) surface.

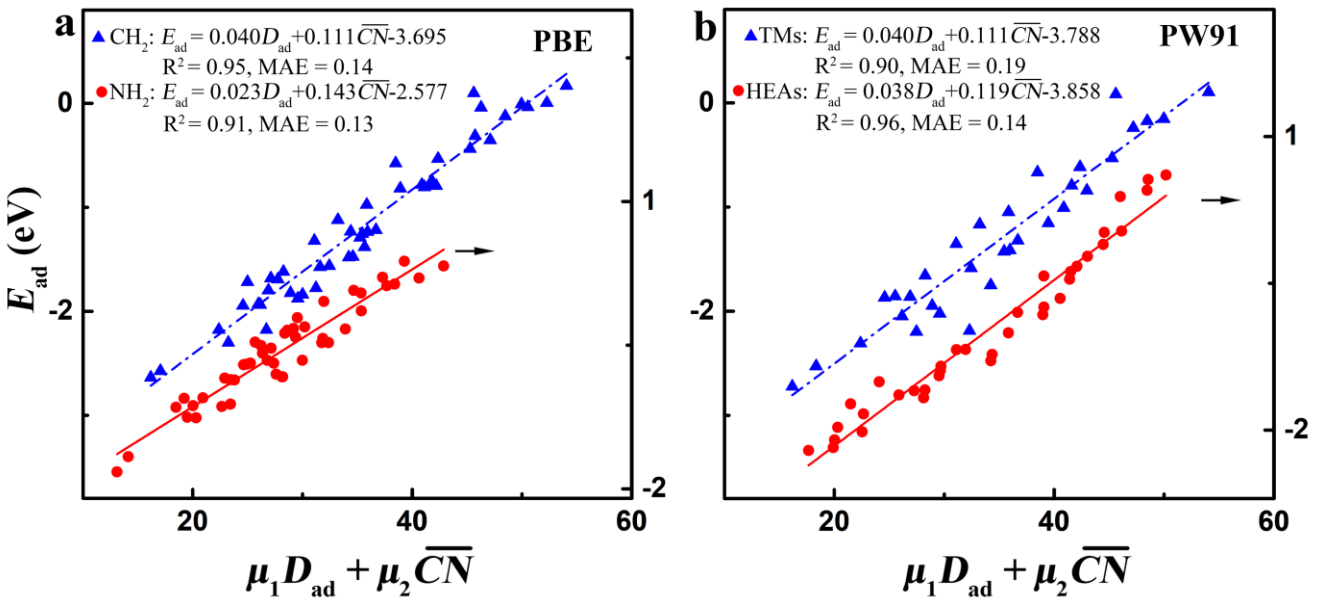

Figure S14. Adsorption energies of the different adsorbates against the electronic and geometric descriptors on TMs and HEAs. (a), CH_2 and NH_2 adsorption at the top site of TM(111) surface with (3 × 3) supercell in dissolution obtained by PBE functional. (b), CH_2 adsorption at the top site of TM(111) surface with (2 × 2) supercell and RuRhIrPdPt-based HEA(111) surface with (4 × 4) supercell in dissolution in the adsorption-site effect of alloying obtained by PW91 functional.

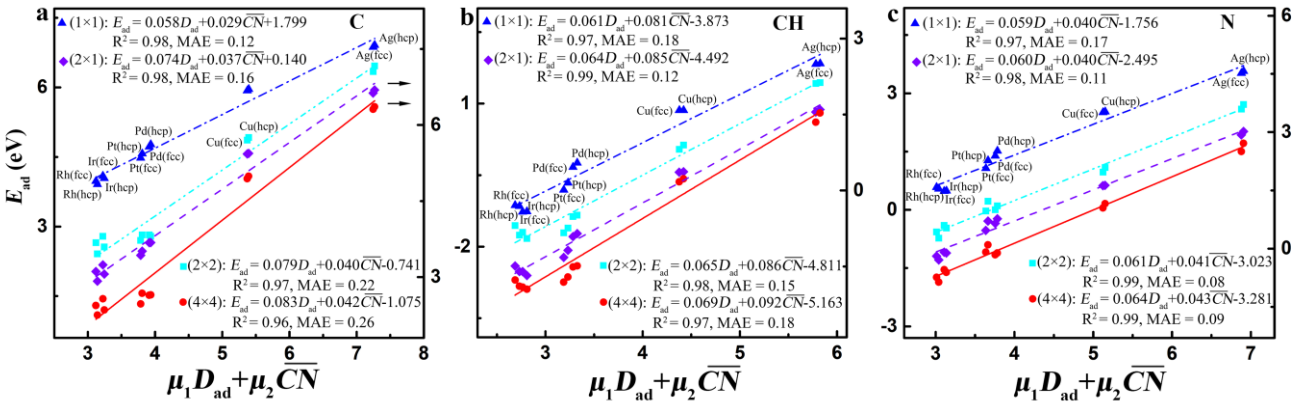

Figure S15. Adsorption energies of the different adsorbates against the electronic and geometric descriptors on TM(111) surface with (1 × 1), (2 × 1), (2 × 2), and (4 × 4) supercells[10]. (a), C. (b), CH. (c), N. All data are calculated with BEEF-vdW functional.

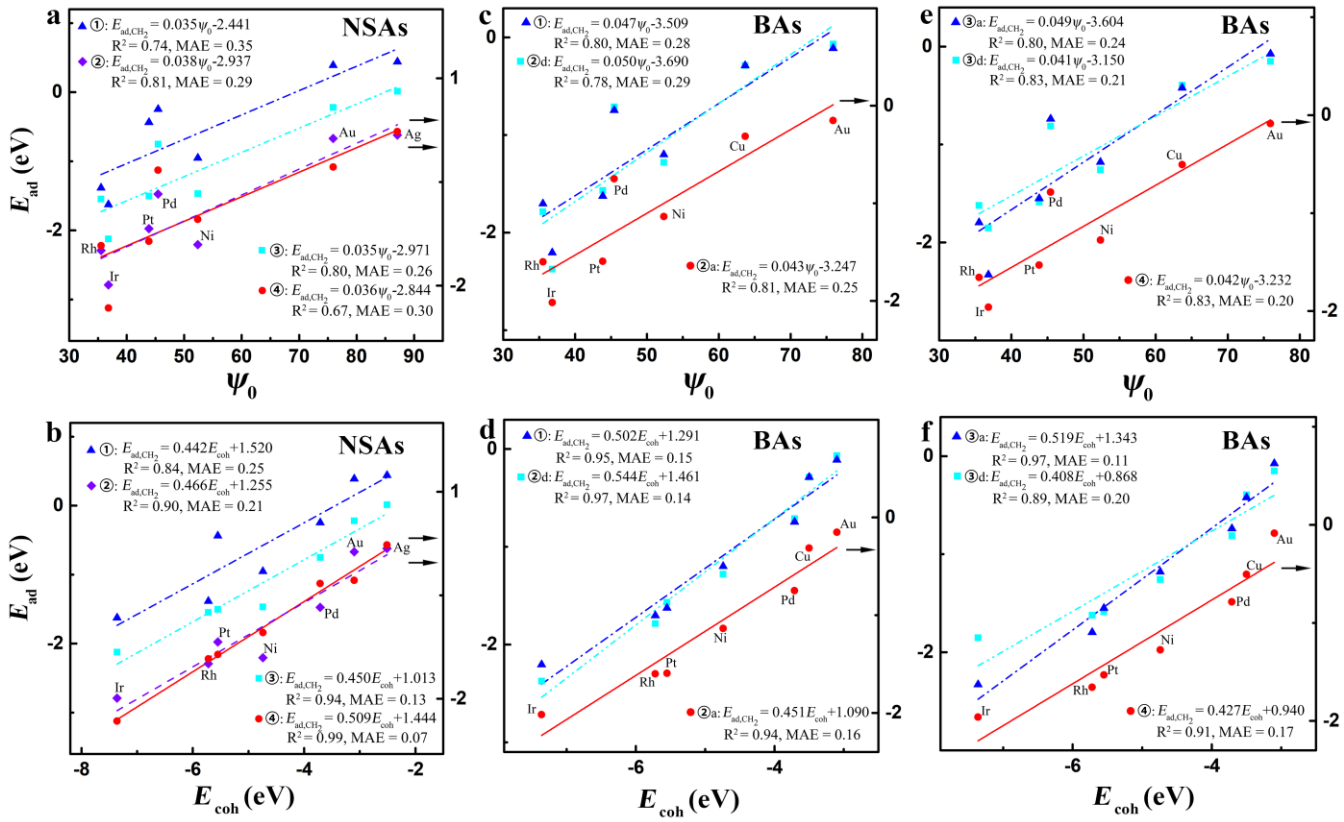

Figure S16. Comparison between the electronic descriptor ψ_0 and cohesive energy E_{coh} in describing the adsorption energy of CH_2 on (111) surface of CuM NSAs (a) and (b), and (100) surface of AgM BAs (c-f) in dissolution with (2 × 2) supercell. All data are calculated by PBE functional.

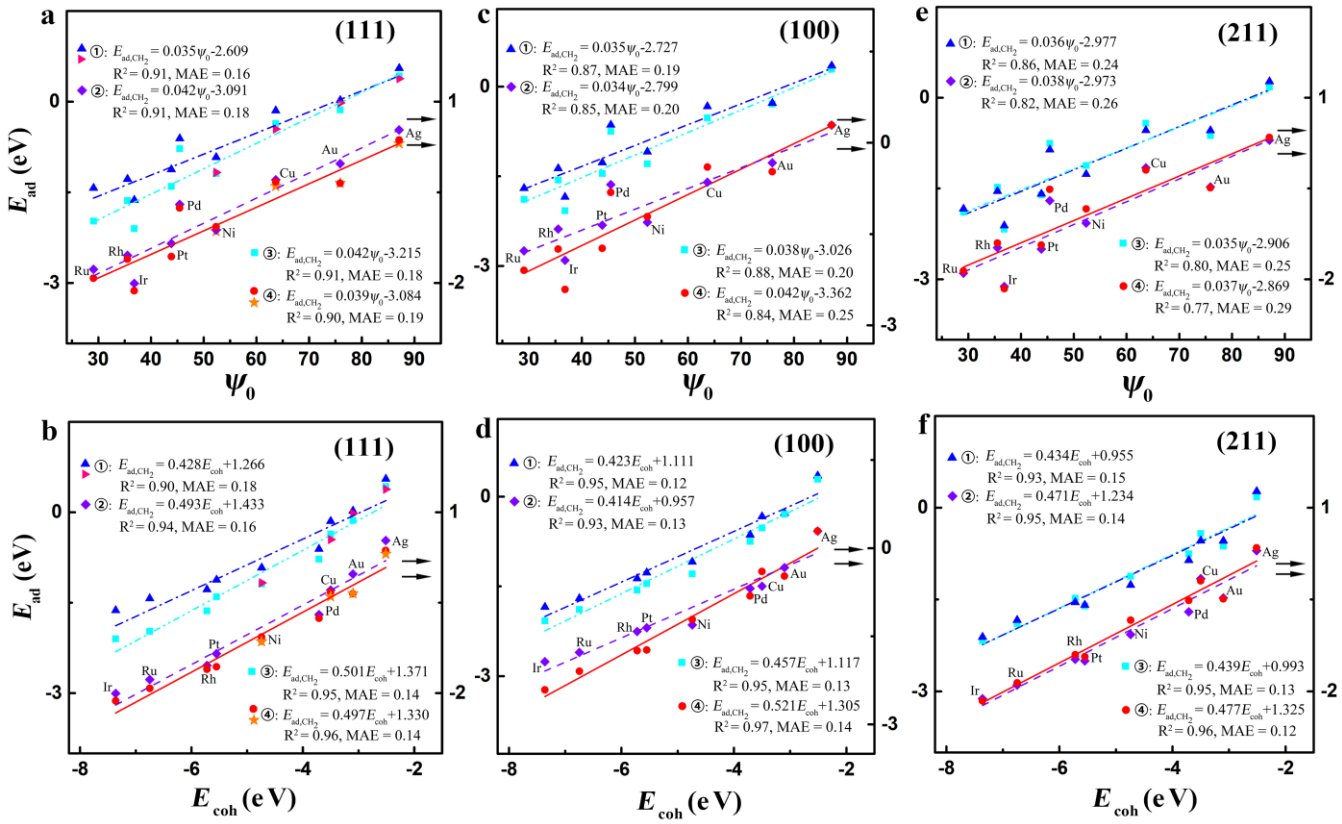

Figure S17. Comparison between the electronic descriptor ψ_0 and cohesive energy E_{coh} in describing the adsorption energy of CH_2 on RuRhIrPdPt-based HEAs in dissolution. (a) and (b), (111) surface with (4 × 4) supercell. (c) and (d), (100) surface with (4 × 4) supercell. (e) and (f), (211) surface with (2× 4) supercell. All data are calculated by PBE functional. In (a) and (b), the pink triangle and orange star icons represent the case that changing all the elements that are the same as the adsorption site while the rest do the case that changing only the element of the adsorption site.

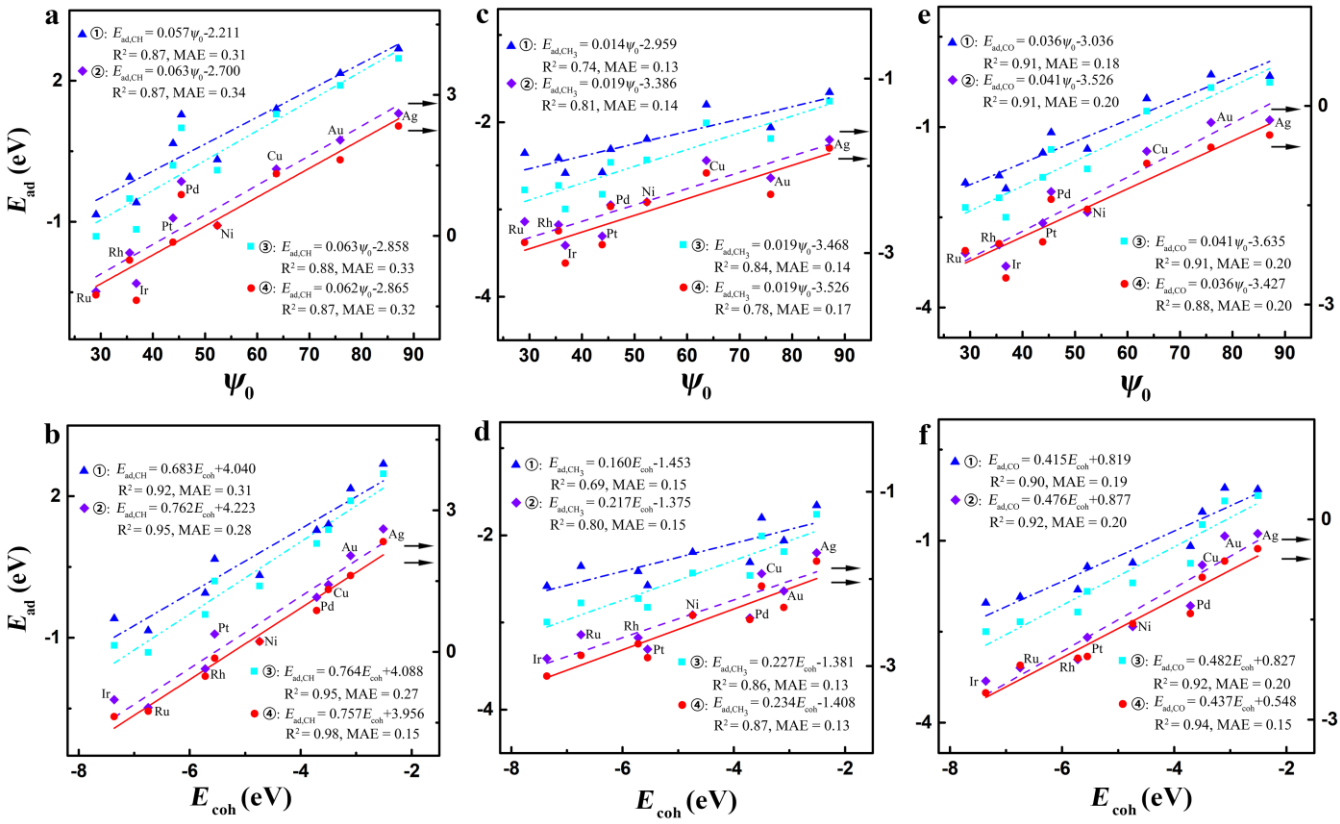

Figure S18. Comparison between the electronic descriptor ψ_0 and cohesive energy E_{coh} in describing the adsorption energy of CH, CH_3, and CO on (111) surface of RuRhIrPdPt-based HEAs in dissolution with (4 × 4) supercell. (a) and (b), CH. (c) and (d), CH_3. (e) and (f), CO. All data are calculated by PBE functional.

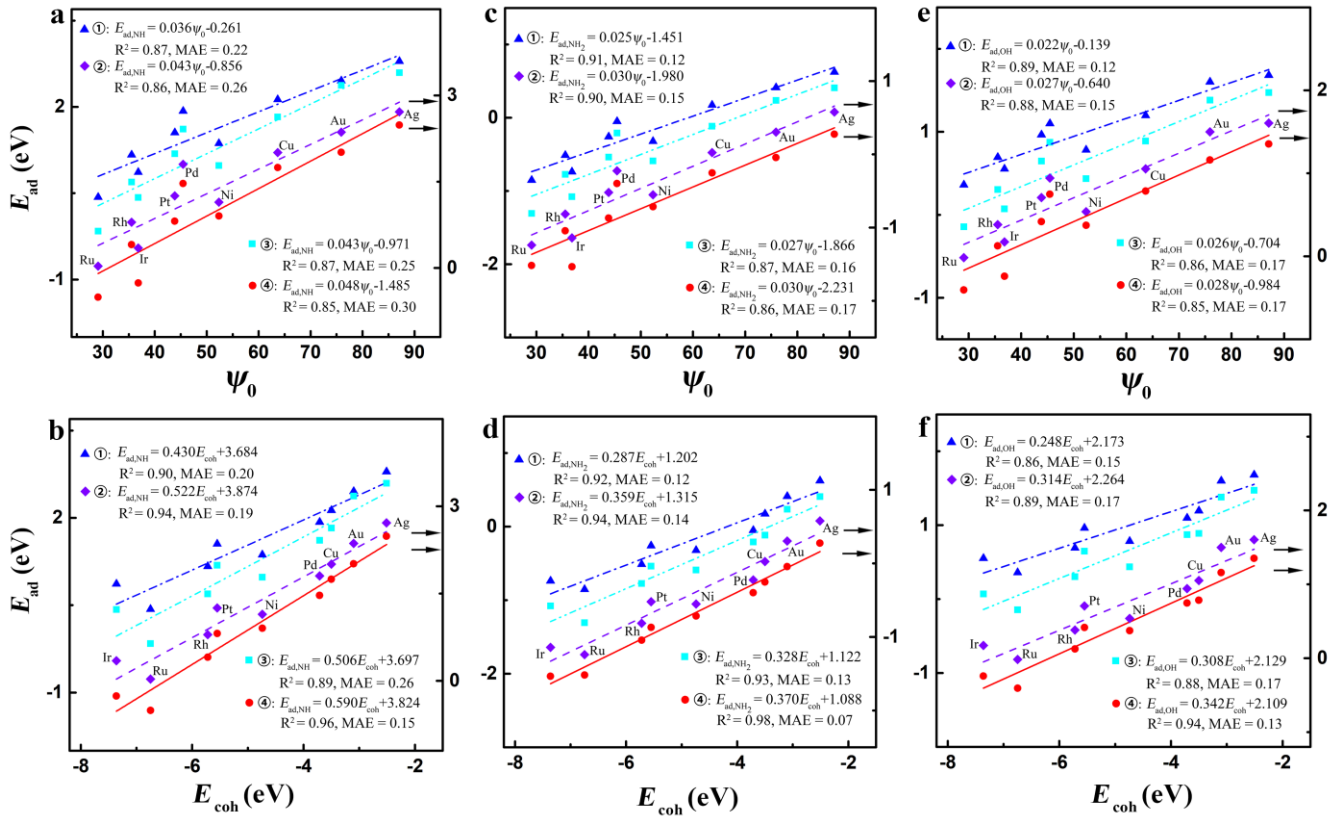

Figure S19. Comparison between the electronic descriptor ψ_0 and cohesive energy E_{coh} in describing the adsorption energy of NH, NH_2, and OH on (111) surface of RuRhIrPdPt-based HEAs in dissolution with (4 × 4) supercell. (a) and (b), NH. (c) and (d), NH_2. (e) and (f), OH. All data are calculated by PBE functional.

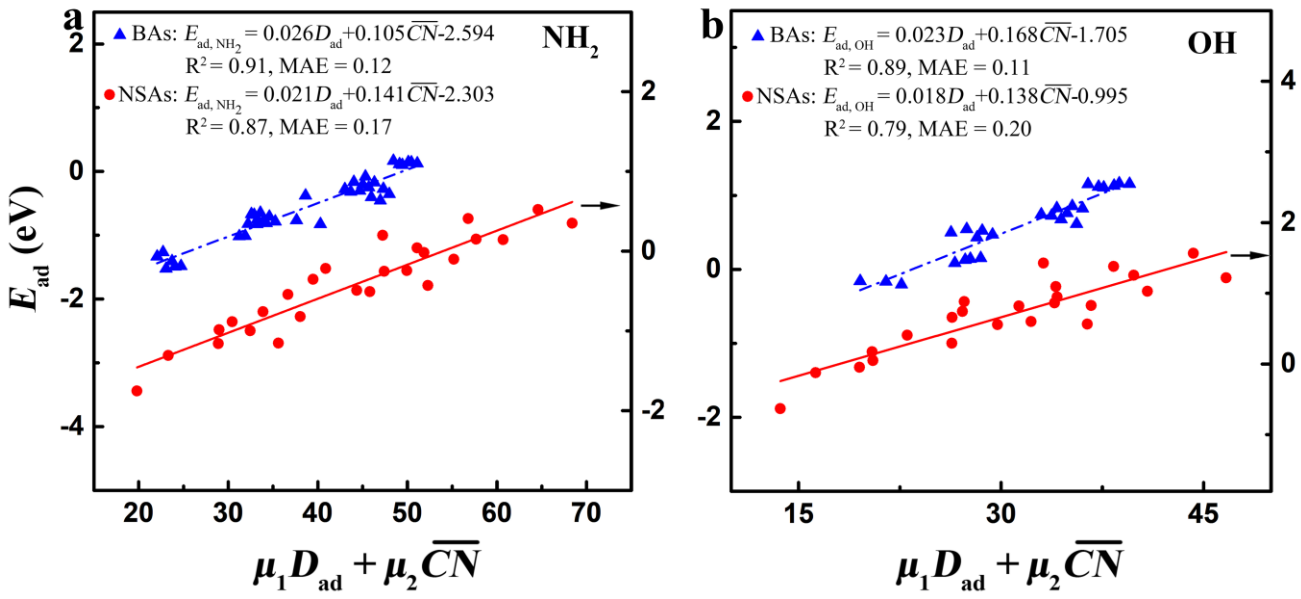

Figure S20. Adsorption energies of NH_2 and OH against the electronic and geometric descriptors at the top site of (100) surface of AgM BAs and (111) surface of CuM NSAs in dissolution with (2 × 2) supercell in the adsorption-site effect of alloying. (a), NH_2. (b), OH. All data are calculated by PBE functional.

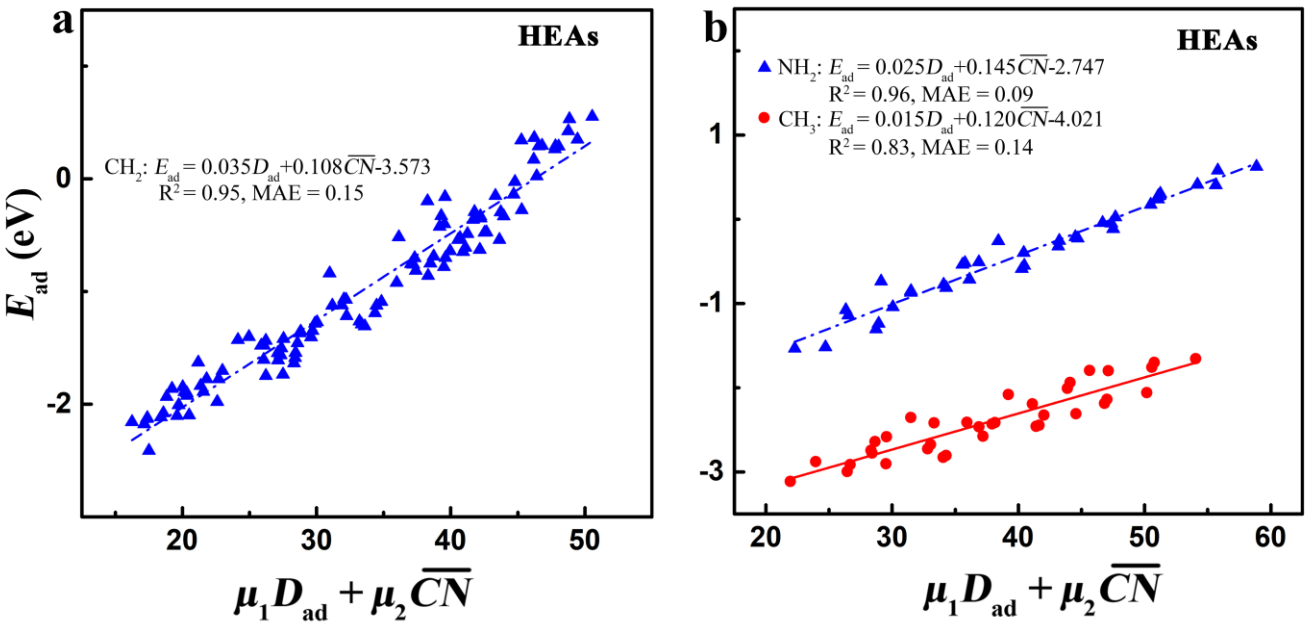

Figure S21. Adsorption energies of the different adsorbates in dissolution against the electronic and geometric descriptors at the top site of RuRhIrPdPt-based HEAs in the adsorption-site effect of alloying. (a), CH_2 adsorption on (111), (100), and (211) surfaces of HEAs. (b), NH_2 and CH_3 adsorption on (111) surface of HEAs. All data are calculated by PBE functional. Note that (111) and (100) surfaces are modeled by (4 × 4) supercell while (211) surface is modeled by (2 × 4) supercell.

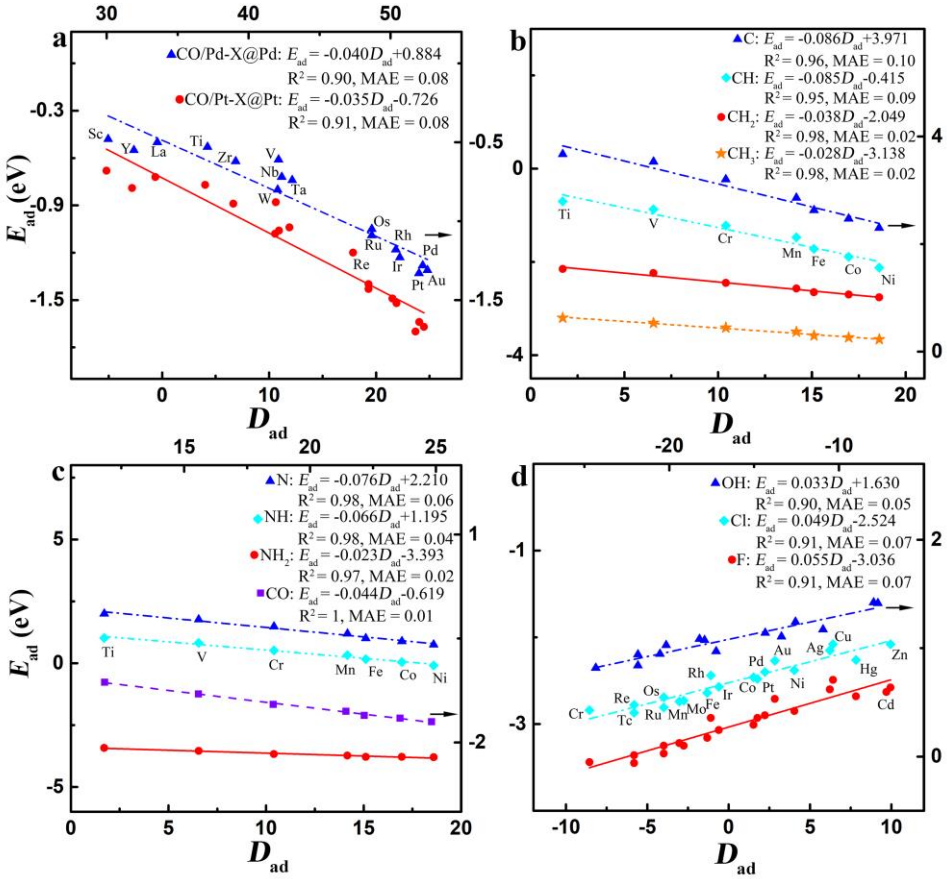

Figure S22. Adsorption energies of the different adsorbates against the electronic descriptor at the top site of PtM and PdM NSAs in the environmental effect of alloying. (a), CO adsorption on (100) surface with (4 × 2) supercell of PtM and PdM NSAs[16]. (b-d), CH_x (x = 0-3), CO, NH_x (x= 0-2)[15], OH[9], F and Cl[17] on (111) surface with (2 × 2) supercell of PtM NSAs. Note that the data for CO, and F and Cl in subfigures (a) and (d) are calculated by PBE functional while those for CH_x (x = 0-3), CO, NH_x (x= 0-2), and OH in subfigures (b-d) are calculated by PW91 functional.

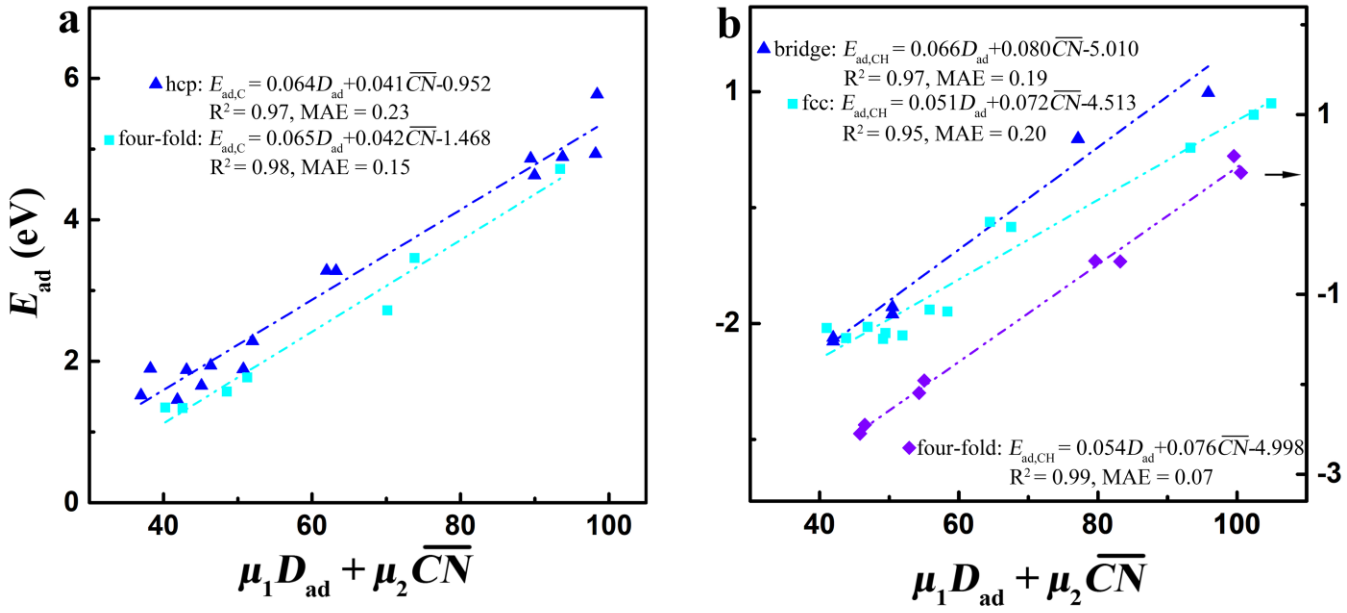

Figure S23. Adsorption energies of C and CH against the electronic and geometric descriptors on AgAu, AgPd, IrRu, and PtRh BAs with the variable adsorption sites and surrounding environments in both the adsorption-site and environmental effects of alloying[12]. (a), C adsorption at the hcp and four-fold sites of the undissolved (211) surface of BAs. (b), CH adsorption at the bridge, fcc, and four-fold sites of the undissolved (211) surface of BAs. All data are calculated by BEEF-vdW functional and (211) surface is modeled by (1 × 2) supercell.

.

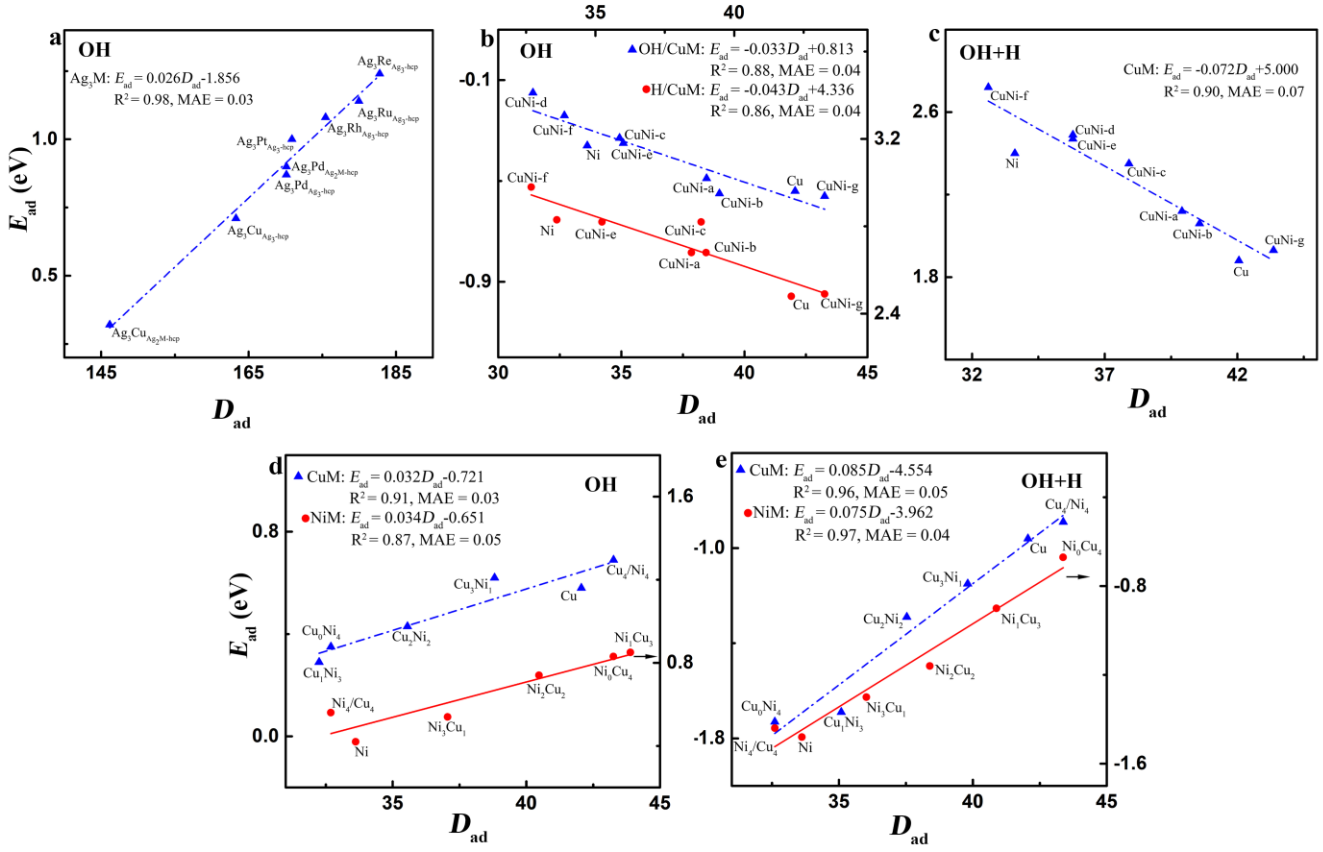

Figure S24. Adsorption energies against the electronic descriptor on (111) surface of BAs and NSAs in both the adsorption-site and environmental effects of alloying. (a), OH adsorption at the different hcp sites of Ag_3M BAs with (2 × 2) supercell obtained by BEEF-vdW functional[18]. (b) and (c), OH and H adsorption and OH + H coadsorption at the fcc sites of Cu, Ni, and CuNi NSAs with (3 × 3) supercell obtained by PW91 functional[13]. NSAs contain the topmost layer with one Ni atom (CuNi-a), two Ni atoms (CuNi-c), three Ni atoms (CuNi-b, CuNi-d, and CuNi-e), and nine Ni atoms (CuNi-f), and the subsurface layer with nine Ni atoms (CuNi-g). (d) and (e), OH adsorption at the fcc sites and OH + H coadsorption at the fcc+hcp sites of Cu, Ni, and CuNi (Cu_xNi_y and Ni_xCu_y) NSAs with (2 × 2) supercell obtained by PBE functional[14]. *x* and *y* denote the corresponding atom numbers in the topmost layer. Cu_4/Ni_4 (Ni_4/Cu_4) denotes the subsurface-layer atoms of Cu (Ni) host are replaced by Ni (Cu) atoms.

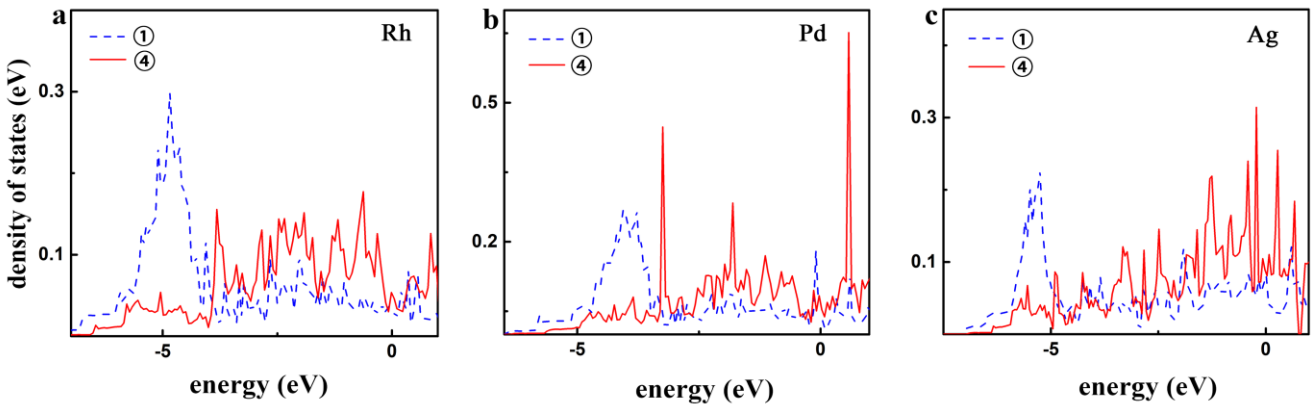

Figure S25. Density of states of the *s* bands of Rh, Pd, and Ag atoms on the undissolved (111) surface (denoted by the symbol ①) and that with three atoms dissolved (denoted by the symbol ④).

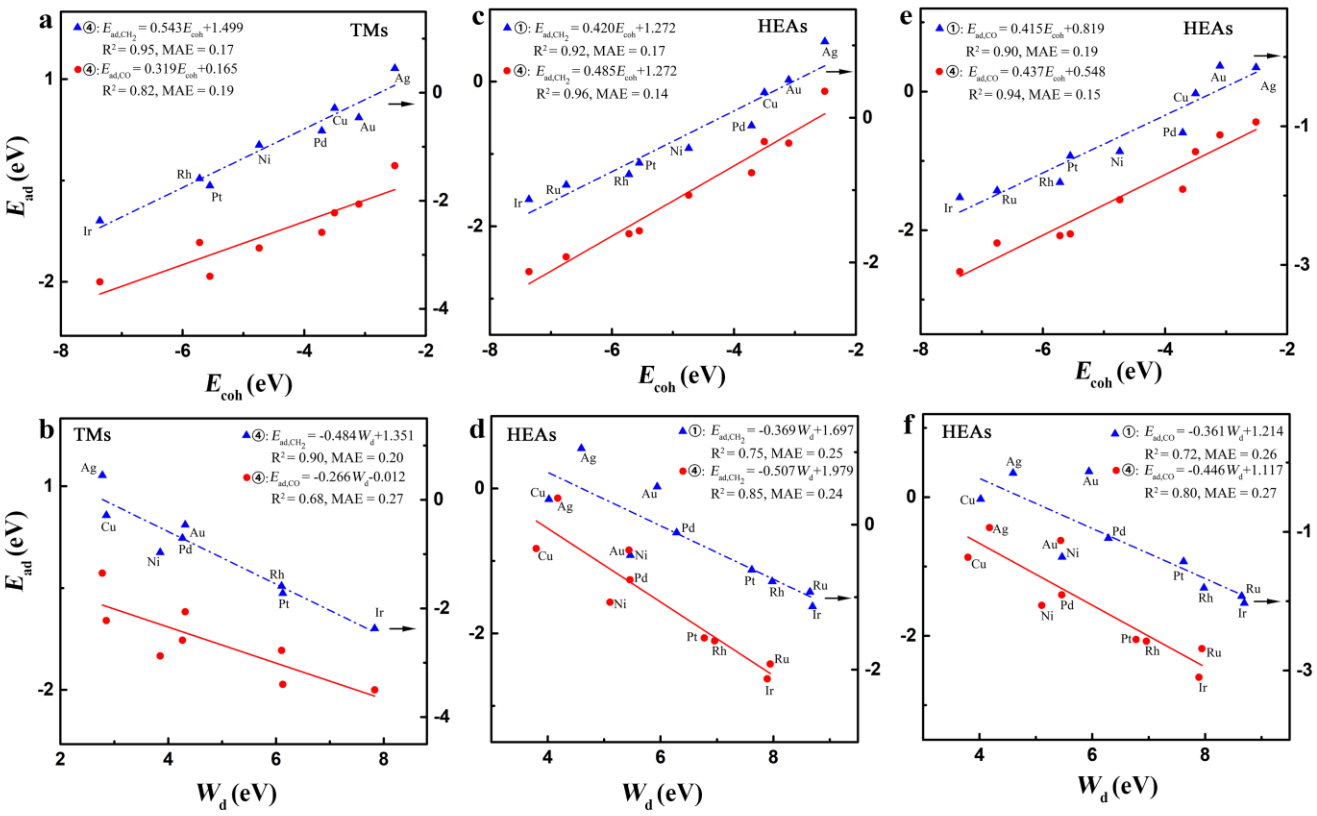

Figure S26. Comparison between the cohesive energy (E_{coh}) and the *d*-band width (W_d) in describing the adsorption energy of CH_2 and CO on (111) surface of TMs and RuRhIrPdPt-based HEAs in dissolution. (a) and (b), CH_2 and CO on the TM(111) surface with three atoms dissolved (④). (c-f), CH_2 and CO on the undissolved HEA(111) surface (①) and that with three atoms dissolved (④). Note that the CO adsorption on TMs is calculated with RPBE functional[11] while the others are calculated with PBE functional.

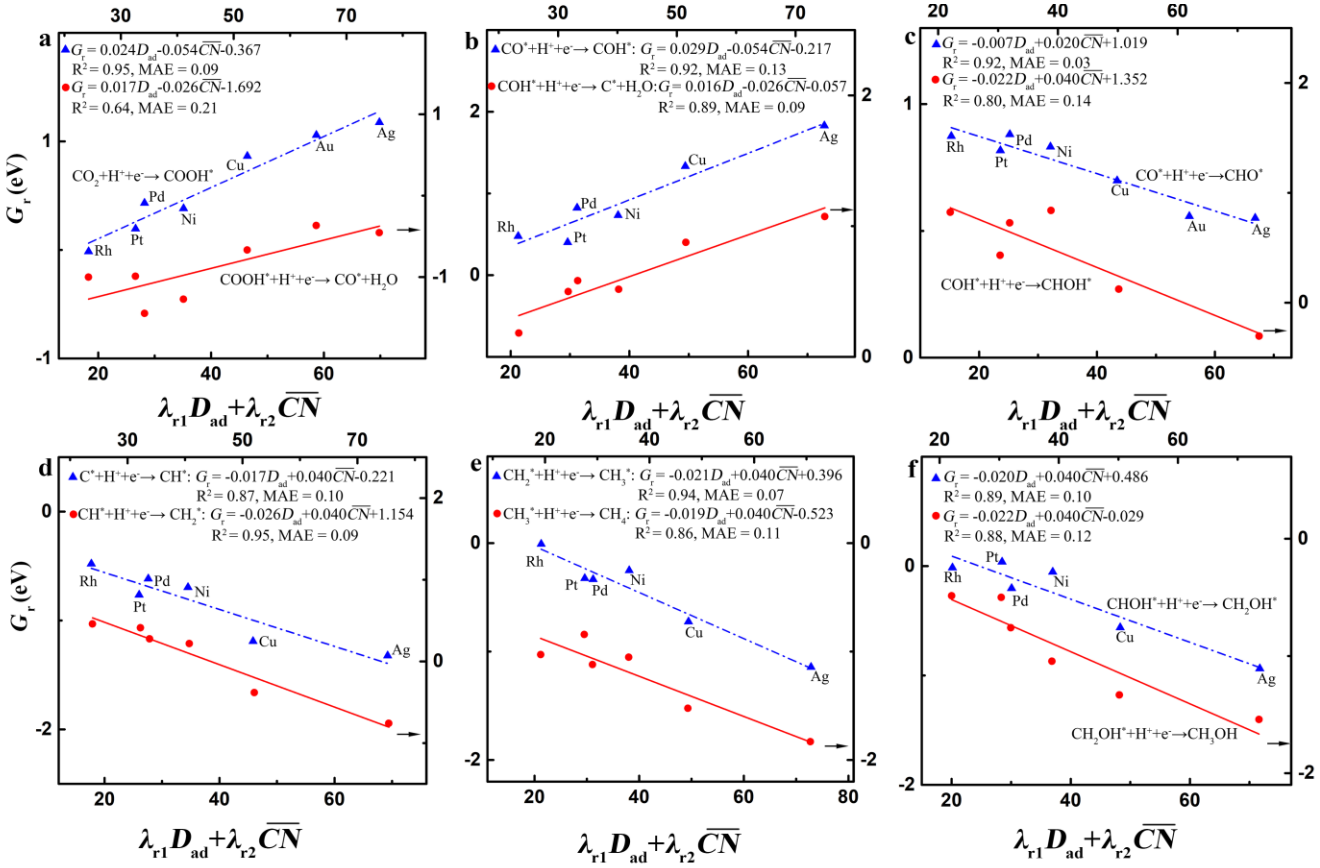

Figure S27. Reaction free energies for the electrochemical reaction, CO_2RR, against the electronic and geometric descriptors at the top site of TM(111) surface[20]. All data are calculated by RPBE functional.

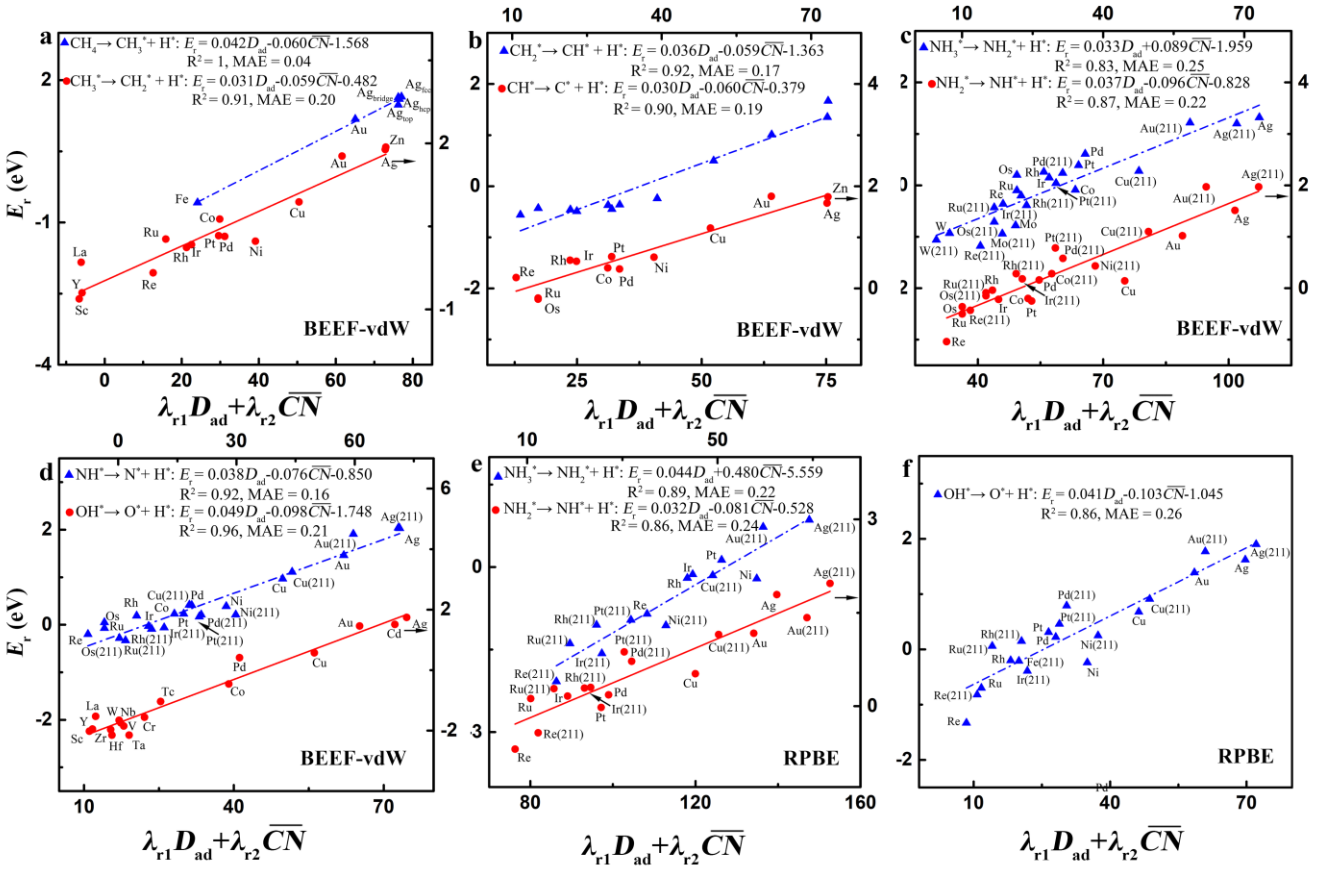

Figure S28. Reaction energies for the thermochemical reactions against the electronic and geometric descriptors on TMs. (a), The decomposition of CH_4[18] and the decomposition of CH_3[25] at the top, bridge, fcc, and hcp sites of close-packed surfaces. (b), The decomposition of CH_2 and CH at the bridge, fcc, and hcp sites of close-packed surfaces[25]. (c), The decomposition of NH_3 at the top site and the decomposition of NH_2 at the bridge site of close-packed and (211) surfaces[23]. (d), The decomposition of NH at the bridge, fcc, hcp, and four-fold sites of close-packed and (211) surfaces[23] and the decomposition of OH at the bridge, fcc and hcp sites of (111) surface[18]. (e), The decomposition of NH_3 at the top site and the decomposition of NH_2 at the bridge site of (111) and (211) surfaces[19]. (f), The decomposition of OH at the fcc site of (111) and (211) surfaces[19]. The data in (a-d) are obtained by BEEF-vdW functional while those in (e) and (f) are obtained by RPBE functional. All data are accessible at https://www.catalysis-hub.org/energies.

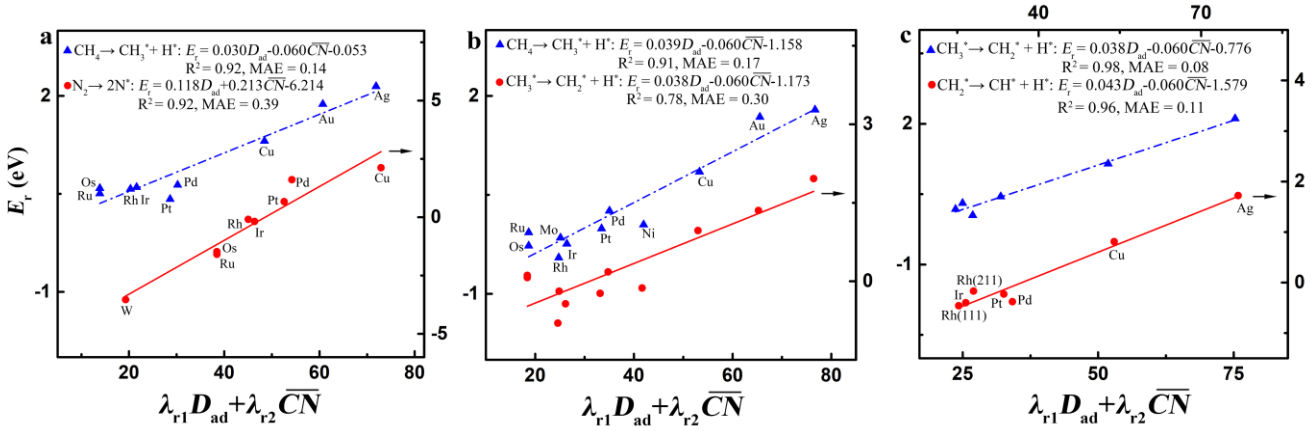

Figure S29. Reaction energies for the thermochemical reactions against the electronic and geometric descriptors on TMs. (a), The decomposition of CH_4 at the top site of close-packed surfaces obtained by RPBE functional[21], and the decomposition of N_2 at the fcc and hcp sites of close-packed surfaces obtained by BEEF-vdW functional[23]. (b), The decomposition of CH_4 and CH_3 at the top site of (100) surface obtained by PW91 functional[22]. (c), The decomposition of CH_3 and CH_2 at the top, bridge, and fcc sites of (111) and (211) surfaces obtained by BEEF-vdW functional[24].

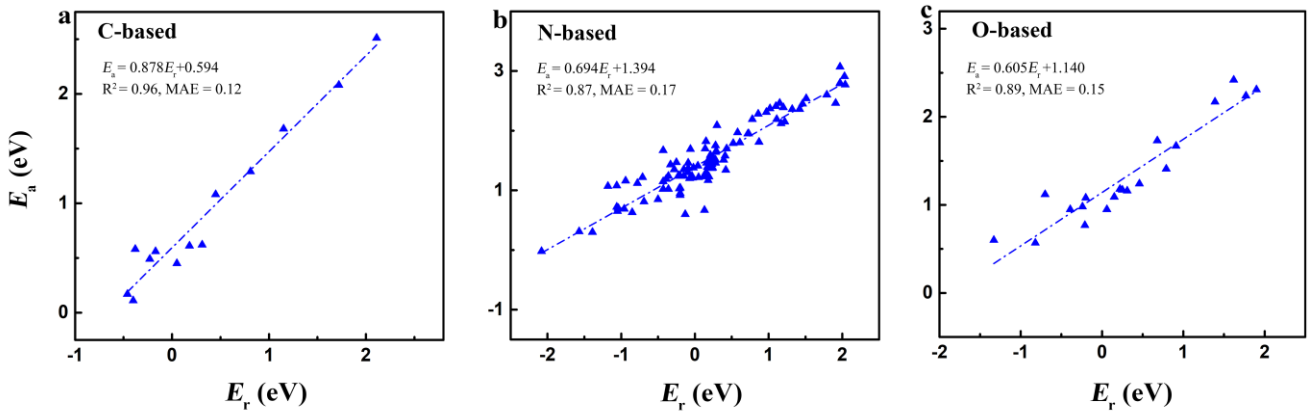

Figure S30. BEP relation of the decomposition of CH_4, NH_3 and OH. (a), The reaction of $CH_3^* \rightarrow CH_2^* + H^*$ and $CH_2^* \rightarrow CH^* + H^*$[24]. (b), The reaction of $NH_3^* \rightarrow NH_2^* + H^*$, $NH_2^* \rightarrow NH^* + H^*$, and $NH^* \rightarrow N^* + H^*$[19,23]. (c), The reaction of $OH^* \rightarrow O^* + H^*$[19].

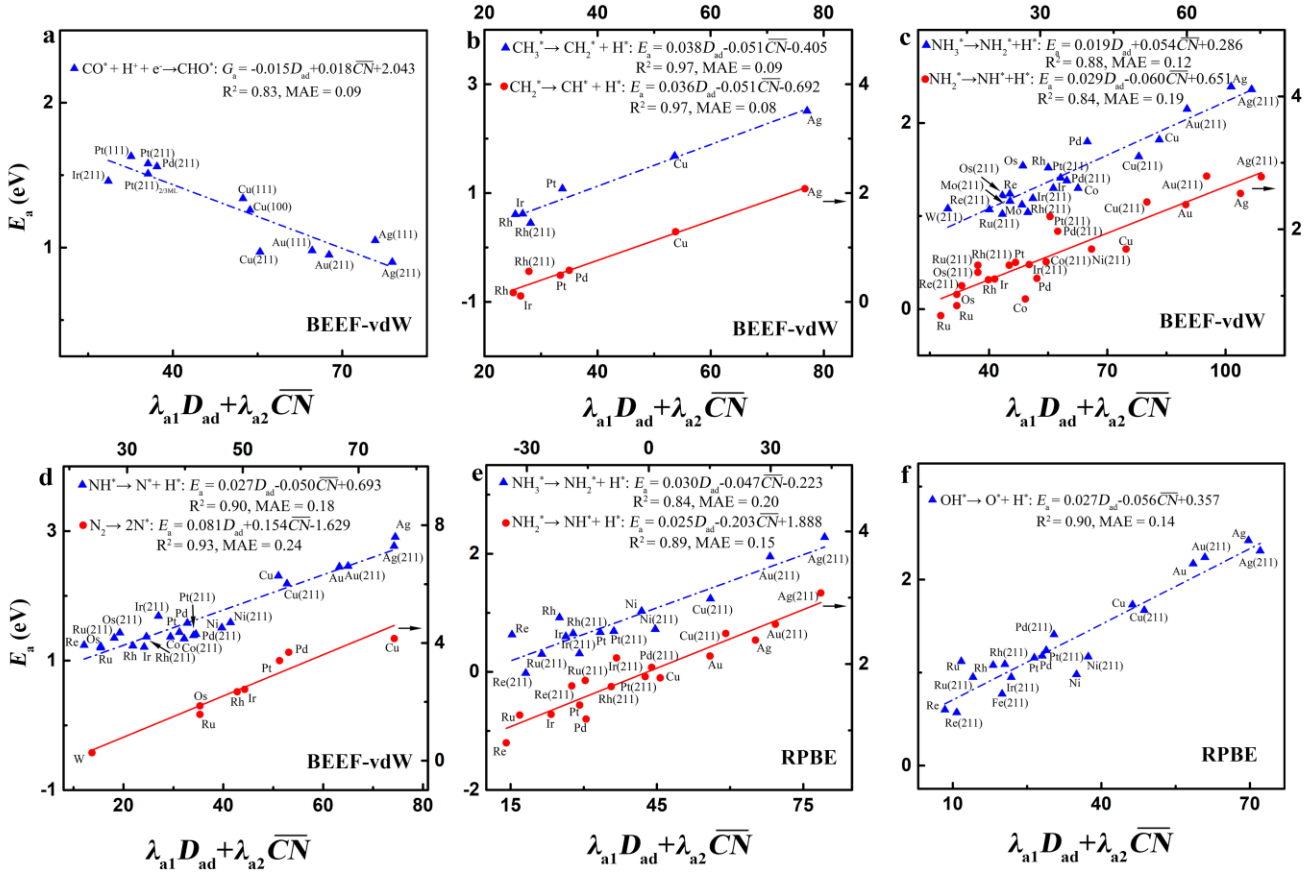

Figure S31. Activation energies for the electrochemical reaction CO_2RR (a) and the thermochemical reactions (b-f) against the electronic and geometric descriptors on TMs. (a), The hydrogenation of CO at the top site[27]. (b), The decomposition of CH_3 at the top site and the decomposition of CH_2 at the bridge and fcc sites of (111) and (211) surfaces[24]. (c), The decomposition of NH_3 at the top site and the decomposition of NH_2 at the bridge site of close-packed and (211) surfaces[23]. (d), The decomposition of NH at the bridge, fcc, hcp, and four-fold sites of close-packed and (211) surfaces, and the decomposition of N_2 at the fcc and hcp sites of close-packed surfaces[23]. (e), The decomposition of NH_3 at the top site and the decomposition of NH_2 at the bridge site of (111) surface and (211) surfaces[19]. (f), The decomposition of OH at the fcc site of (111) and (211) surfaces[19]. The data in (a-d) are obtained by BEEF-vdW functional while those in (e) and (f) are obtained by RPBE functional. All data in (b-f) are accessible at https://www.catalysis-hub.org/energies.

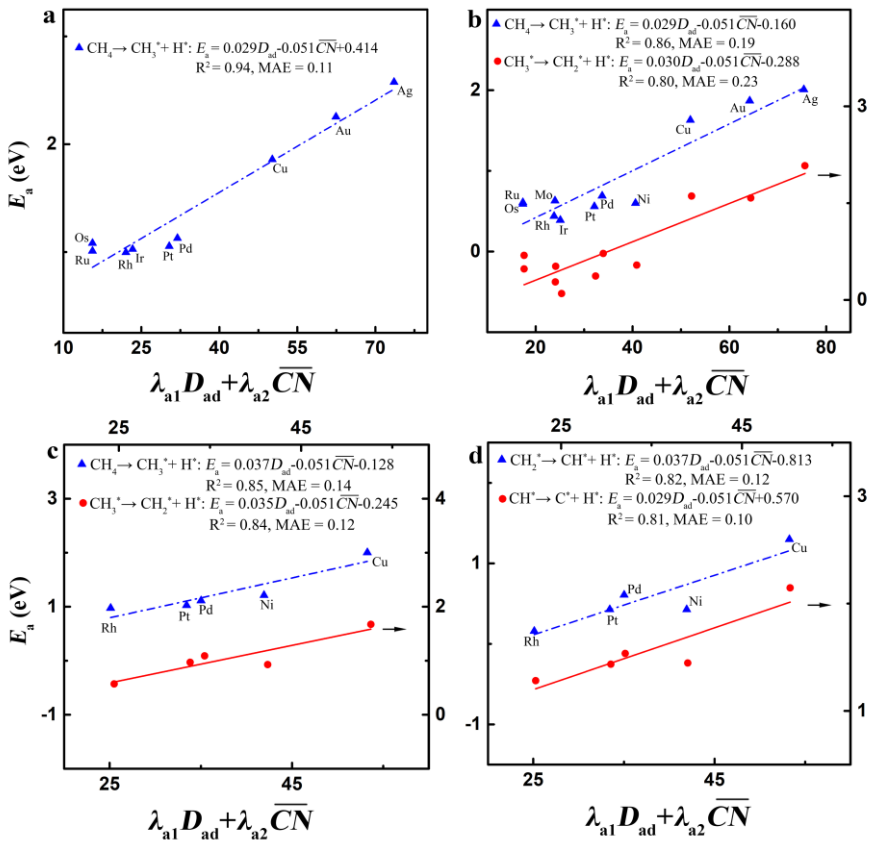

Figure S32. Activation energies for the thermochemical reactions against the electronic and geometric descriptors on TMs. (a), The decomposition of CH_4 at the top site of close-packed surfaces obtained by RPBE functional[21]. (b), The decomposition of CH_4 and CH_3 at the top site of (100) surface obtained by PW91 functional[22]. (c) and (d), The decomposition of CH_4, CH_3, CH_2, and CH at the hcp site of (111) surface obtained by BEEF-vdW functional[29].

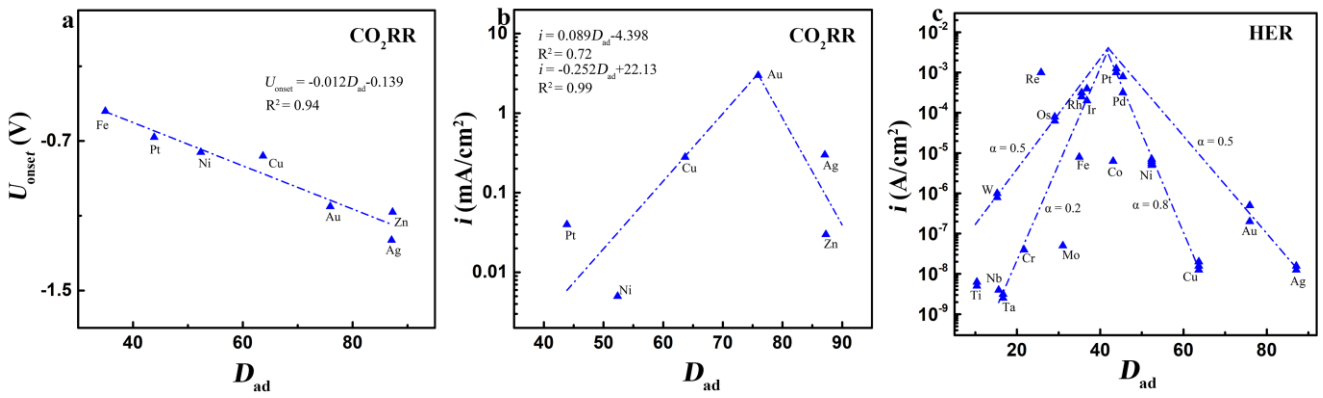

Figure S33. The activity of CO_2RR and HER against the electronic descriptor on TMs. (a), The experimental onset potential for the overall CO_2RR[37,47]. (b), The experimental partial current density for the overall CO_2RR at -0.8 V[37,47]. (c), The experimental exchange current density for HER[30,38,48]. α corresponds to the transfer coefficient.

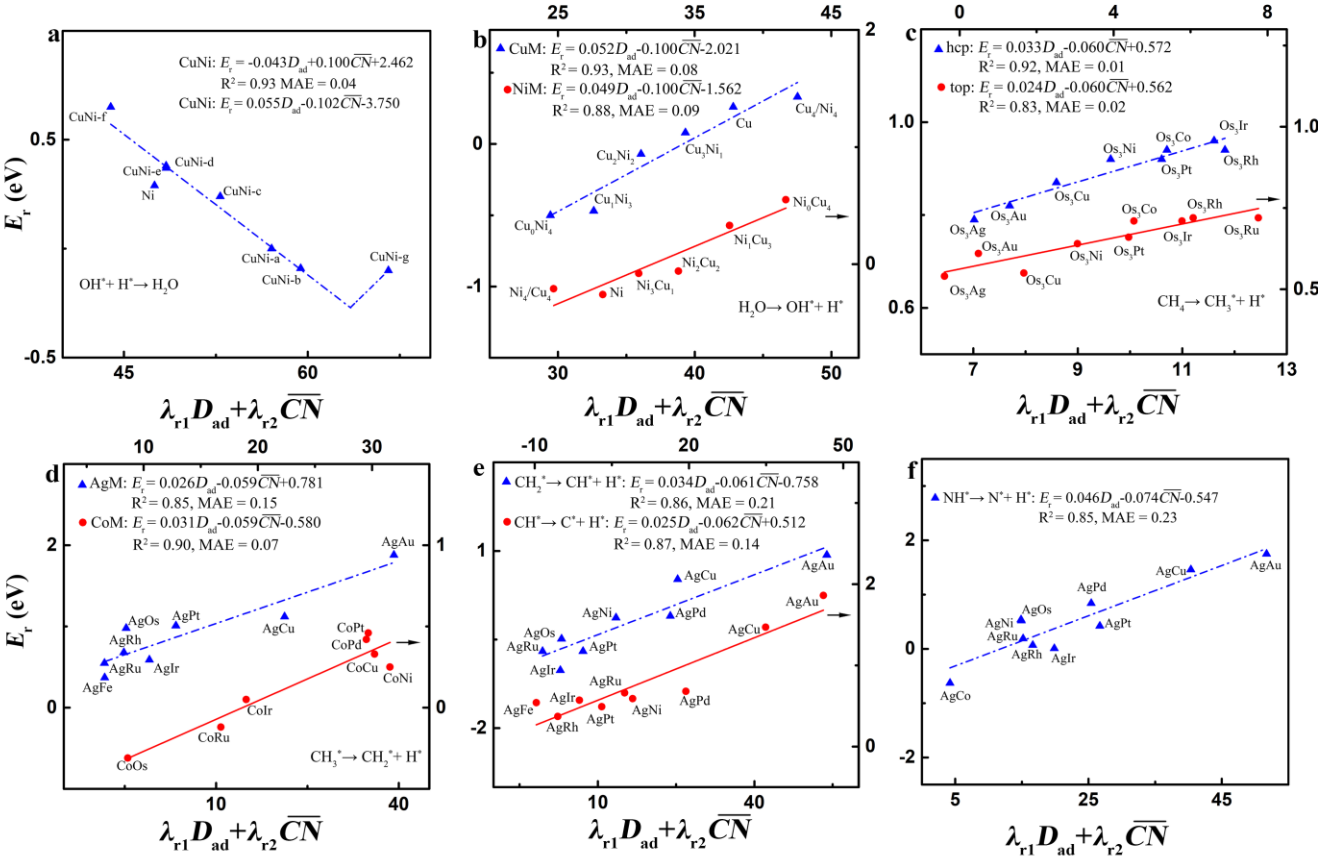

Figure S34. Reaction energies for the thermochemical reactions against the electronic and geometric descriptors on (111) surface of NSAs and BAs. (a), Both OH and H at the fcc site of CuNi NSAs obtained by PW91 functional[13]. NSAs contain the topmost layer with one Ni atom (CuNi-a), two Ni atoms (CuNi-c), three Ni atoms (CuNi-b, CuNi-d, and CuNi-e), and nine Ni atoms (CuNi-f), and the subsurface layer with nine Ni atoms (CuNi-g). (b), OH at the fcc site and H at the hcp site of CuNi (Cu_xNi_y and Ni_xCu_y) NSAs obtained by PBE functional[14]. *x* and *y* denote the corresponding atom numbers in the topmost layer. Cu_4/Ni_4 (Ni_4/Cu_4) denotes the subsurface-layer atoms of Cu (Ni) host are replaced by Ni (Cu) atoms. (c), The decomposition of CH_4 at the top and hcp sites of Os_3M BAs[18]. (d), The decomposition of CH_3 at the top, bridge, fcc, and hcp sites of AgM and CoM BAs[18]. (e), The decomposition of CH_2 at the top, bridge, and hcp sites and the decomposition of CH at the bridge, fcc, and hcp sites of AgM BAs[18]. (f), The decomposition of NH at the top, bridge, fcc, and hcp sites of AgM BAs[18]. All data in (c-f) are obtained by BEEF-vdW functional and are accessible at https://www.catalysis-hub.org/energies.

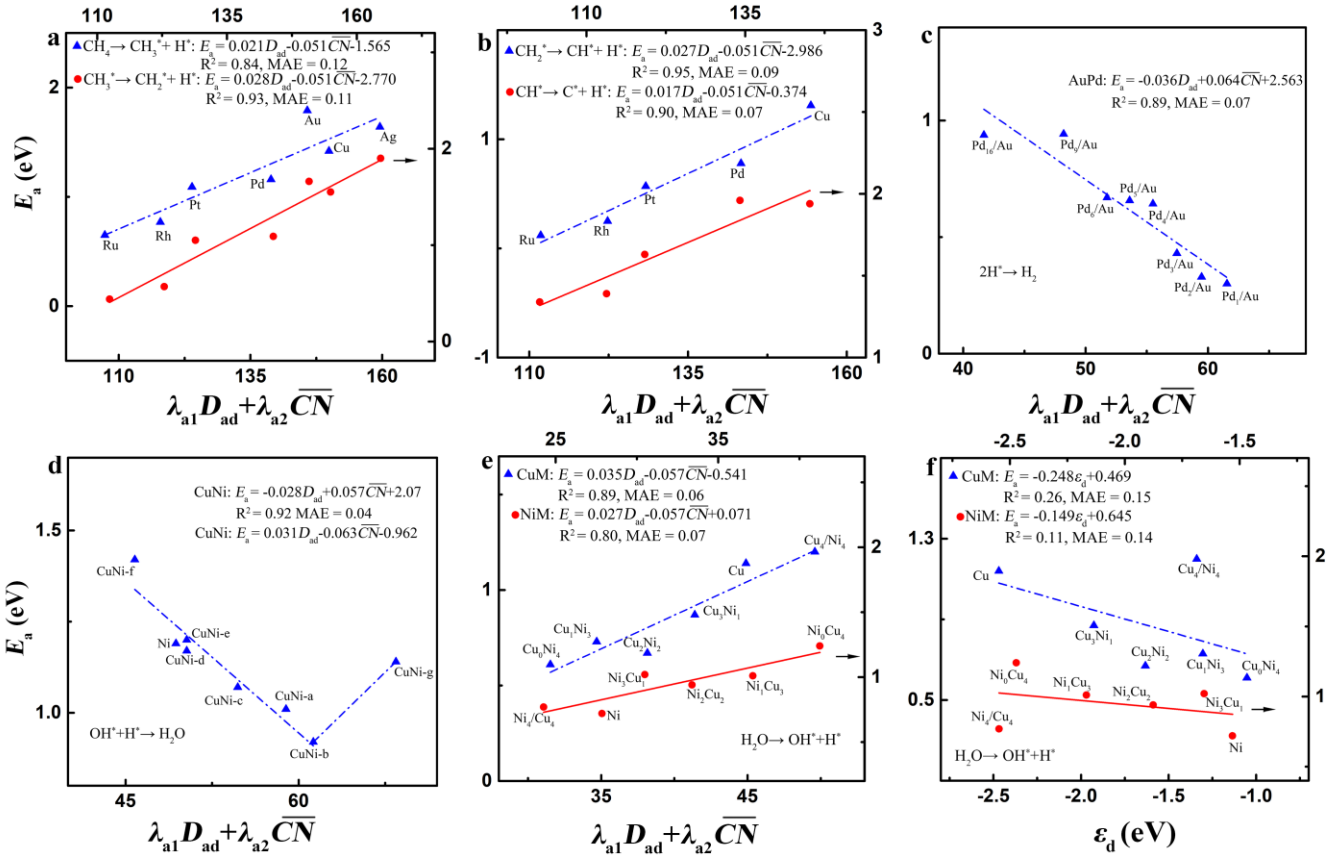

Figure S35. Activation energies for thermochemical reactions against the electronic and geometric descriptors D_{ad} and $\overline{CN}$ or the *d*-band center (ε_d) on (111) surface of NSAs. (a) and (b), The decomposition of CH_4, CH_3, CH_2, and CH at the hcp site (Ni_2M site) of NiM NSAs obtained by PBE functional[28]. (c) H at the fcc site of AuPd NSAs with the different ratio of Pd ensembles in the topmost layer[26] obtained by PBE functional via van der Waals correction (DFT-D3)[49]. (d), Both OH and H at the fcc site of CuNi NSAs obtained by PW91 functional[13]. NSAs contain the topmost layer with one Ni atom (CuNi-a), two Ni atoms (CuNi-c), three Ni atoms (CuNi-b, CuNi-d, and CuNi-e), and nine Ni atoms (CuNi-f), and the subsurface layer with nine Ni atoms (CuNi-g). (e) and (f), Comparison between the $\lambda_1 D_{ad} + \lambda_2 \overline{CN}$ and ε_d in describing the activation energy. OH at the fcc site and H at the hcp site of CuNi (Cu_xNi_y and Ni_xCu_y) NSAs obtained by PBE functional[14]. *x* and *y* denote the corresponding atom numbers in the topmost layer. Cu_4/Ni_4 (Ni_4/Cu_4) denotes the subsurface-layer atoms of Cu (Ni) host are replaced by Ni (Cu) atoms.

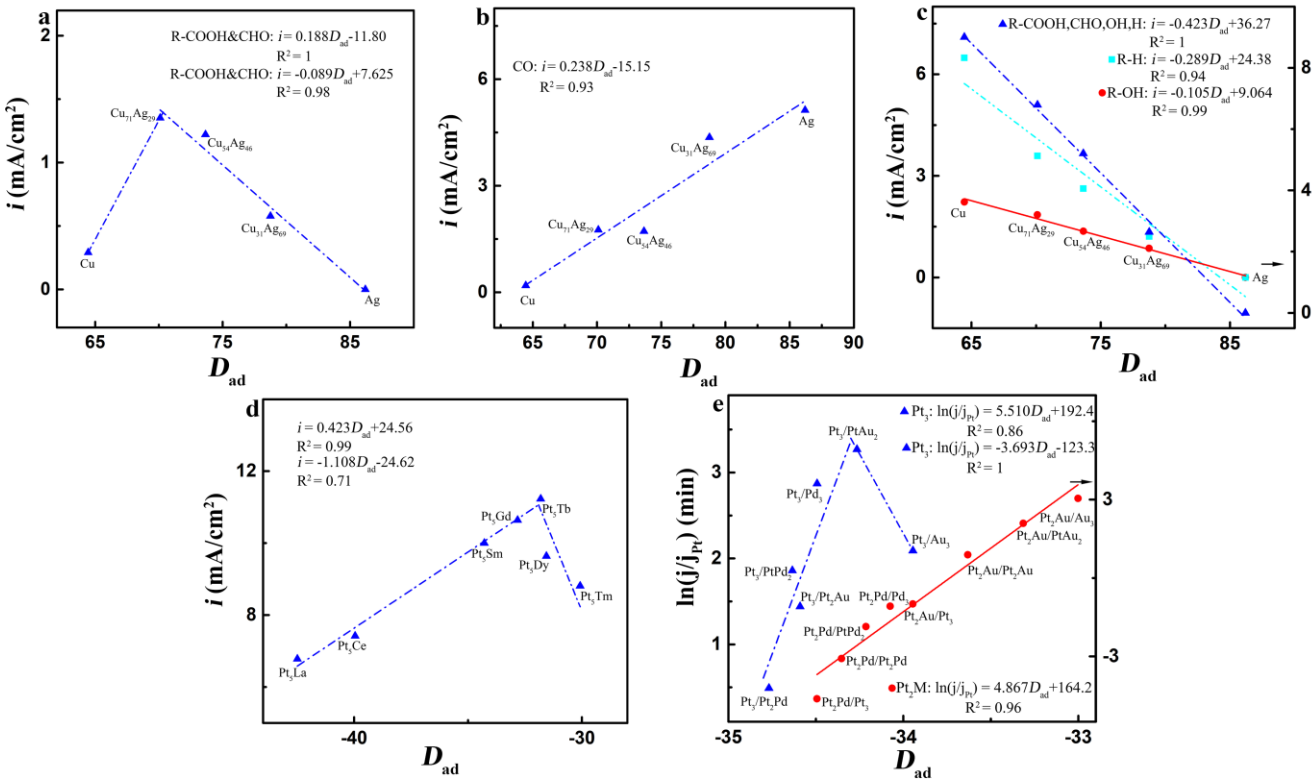

Figure S36. The activity of CO_2RR and ORR against the electronic descriptor on BAs and NSAs. (a-c), The experimental partial current density for the R-COOH, R-CHO, CO, R-H, and R-OH production of CO_2RR at -1.05 V vs. RHE on Cu, Ag, and CuAg BAs. R-X denotes the product that containing the X-group (COOH, CHO, H, and OH) during the CO_2RR process[35]. (d), The experimental kinetic current density of ORR at 0.9 V vs. RHE on La-series Pt_5M BAs. Note that the 4*f*-, 5*d*- and 6*s*-electrons of La-series metals are considered as valence electrons[39]. (e), The DFT-calculated activity of ORR on PtM NSAs with A_xB_{3-x}/A_yB_{3-y} monolayers. A_xB_{3-x} (A_yB_{3-y}) corresponds to the first (second) layer on Pt(111) host and the subscripts *x* and *y* denote the stoichiometry of the corresponding atoms[36]. Note that the electronic descriptor for the experimental results is obtained by using the geometric average of the stoichiometric ratio of the different components as the specific surface sites are uncertain.

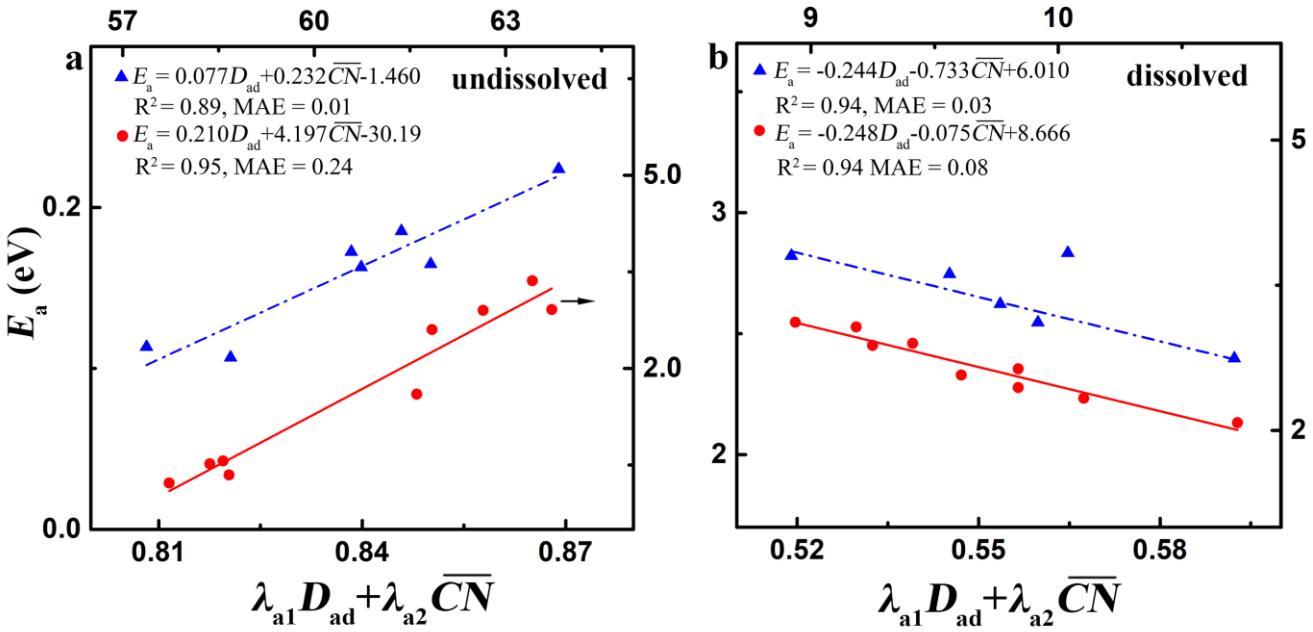

Figure S37. Activation energies of $CH_2^* \rightarrow CH^* + H^*$ reaction against the electronic and geometric descriptors on (111) surface of RuRhIrPdPt-based HEAs with (4 × 4) supercell. (a), Reactions on undissolved (111) surface. The blue line contains the unchanged hcp sites of reactants and products, while the red line does the changed sites from the top and bridge sites of reactants to fcc sites of products and from the bridge and fcc sites of reactants to hcp sites of products. (b), Reactions on (111) surface with three atoms dissolved. The blue line contains the changed sites from the different bridge sites of reactants to fcc sites of products, while the red line does the unchanged top sites of reactants and products and changed sites from bridge sites of reactants to fcc sites of products. The blue triangle denotes the adsorption-site effect of alloying while the red circle does both the adsorption-site and environmental effects of alloying. All data are calculated with PBE functional.

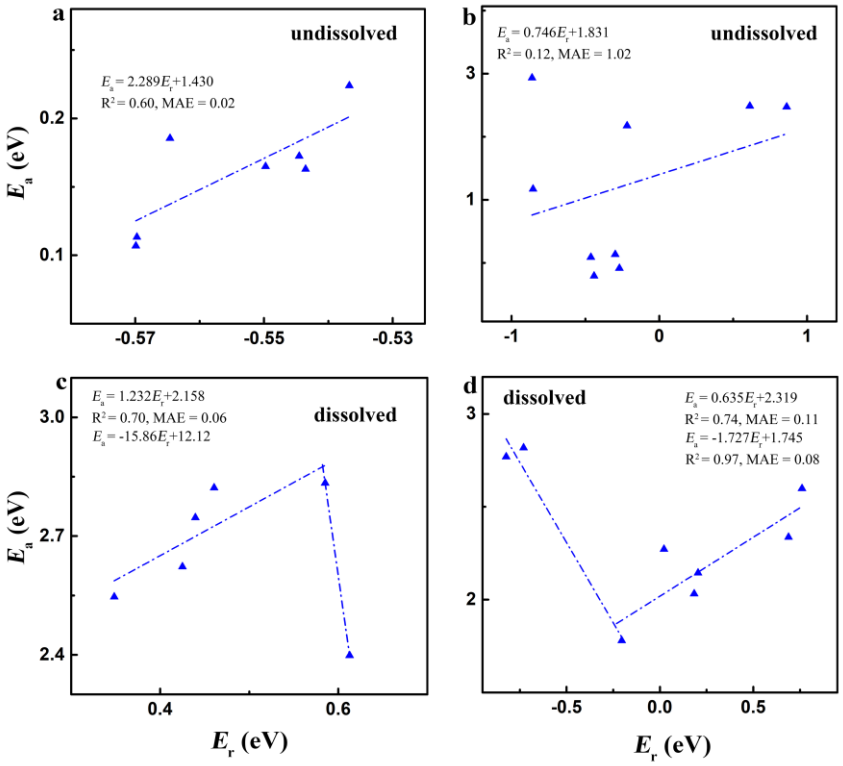

Figure S38. BEP relation of $CH_2^* \rightarrow CH^* + H^*$ reaction on (111) surface of RuRhIrPdPt-based HEAs with (4 × 4) supercell. (a), Undissolved (111) surface in the adsorption-site effect of alloying. (b), Undissolved (111) surface in both the adsorption-site and environmental effects of alloying. (c), (111) surface with three atoms dissolved in the adsorption-site effect of alloying. (d), (111) surface with three atoms dissolved in both the adsorption-site and environmental effects of alloying. All data are calculated with PBE functional.

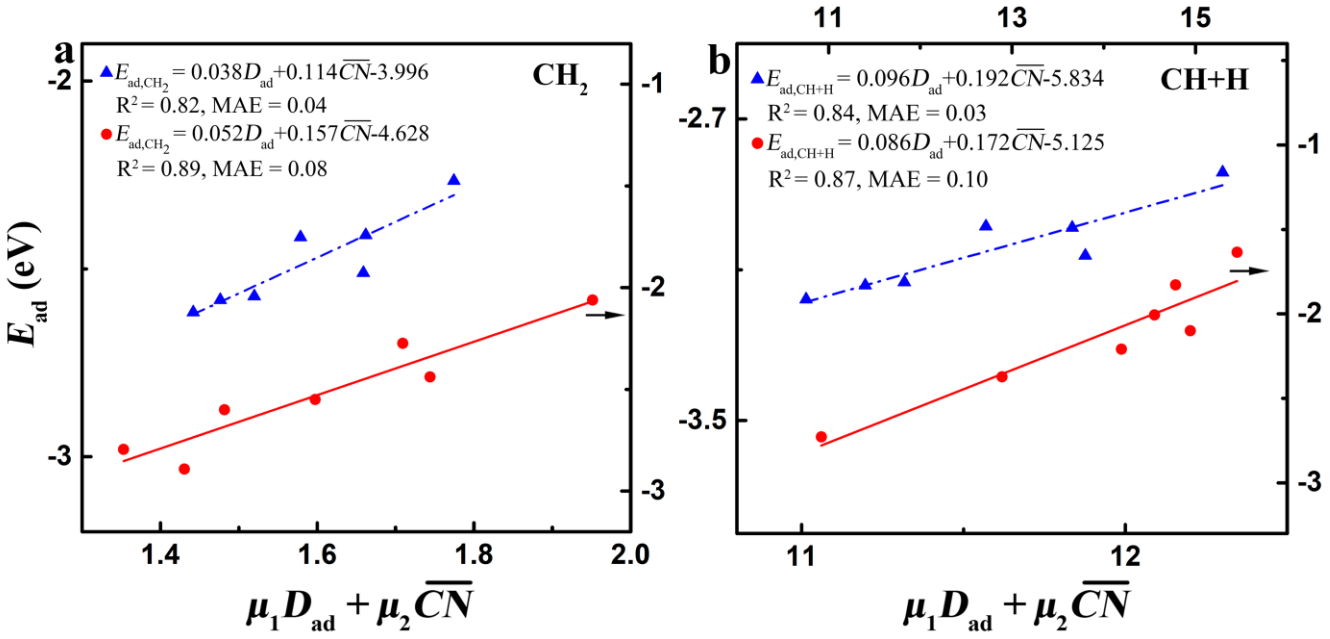

Figure S39. Adsorption energies of CH_2 and CH+H against the electronic and geometric descriptors on RuRhIrPdPt-based HEAs in the adsorption-site effect of alloying. (a), CH_2 adsorption at the hcp site of the undissolved (111) surface (blue triangle) and at the bridge site of (111) surface with three atoms dissolved (red circle). (b), CH and H coadsorption on the undissolved (111) surface (blue triangle) and on the (111) surface with three atoms dissolved (red circle). All data are calculated with PBE functional.

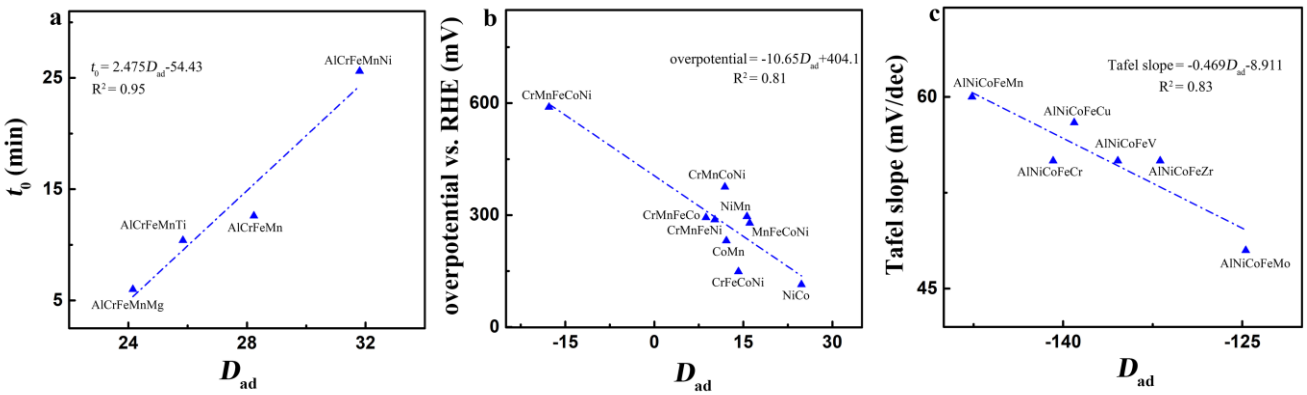

Figure S40. The activity against the electronic descriptor on HEAs. (a), The experimental decoloration time (t_0) of decolorization reaction (corresponding to the reaction efficiency) on AlCrFeMn-based HEAs[31]. (b), The experimental overpotential of ORR at −0.5 V on HEAs and BAs[34]. (c), The experimental Tafel slopes of OER on AlNiCoFe-based HEAs[32]. Note that the electronic descriptor is obtained by using the geometric average of the stoichiometric ratio of the different components as the specific surface sites are uncertain.

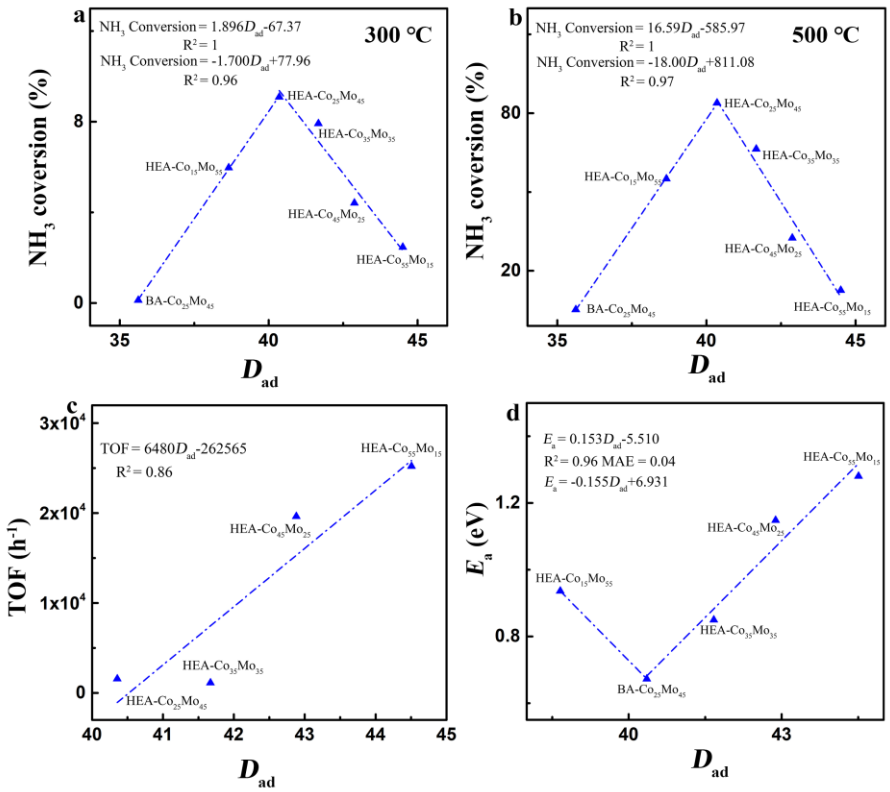

Figure S41. The activity of ammonia decomposition against the electronic descriptor on HEAs[33]. (a) and (b), The experimental NH_3 conversion efficiency under the different reaction temperatures 300℃ and 500℃ on HEAs (HEA-Co_xMo_y) and BAs (BA-Co_xMo_y) with the different Co/Mo ratios. (c), The experimental turnover frequency (TOF) on HEAs with the different Co/Mo ratios. (d), The experimental-estimated activation energy on HEAs with the different Co/Mo ratios. Note that the electronic descriptor is obtained by using the geometric average of the stoichiometric ratio of the different components as the specific surface sites are uncertain.

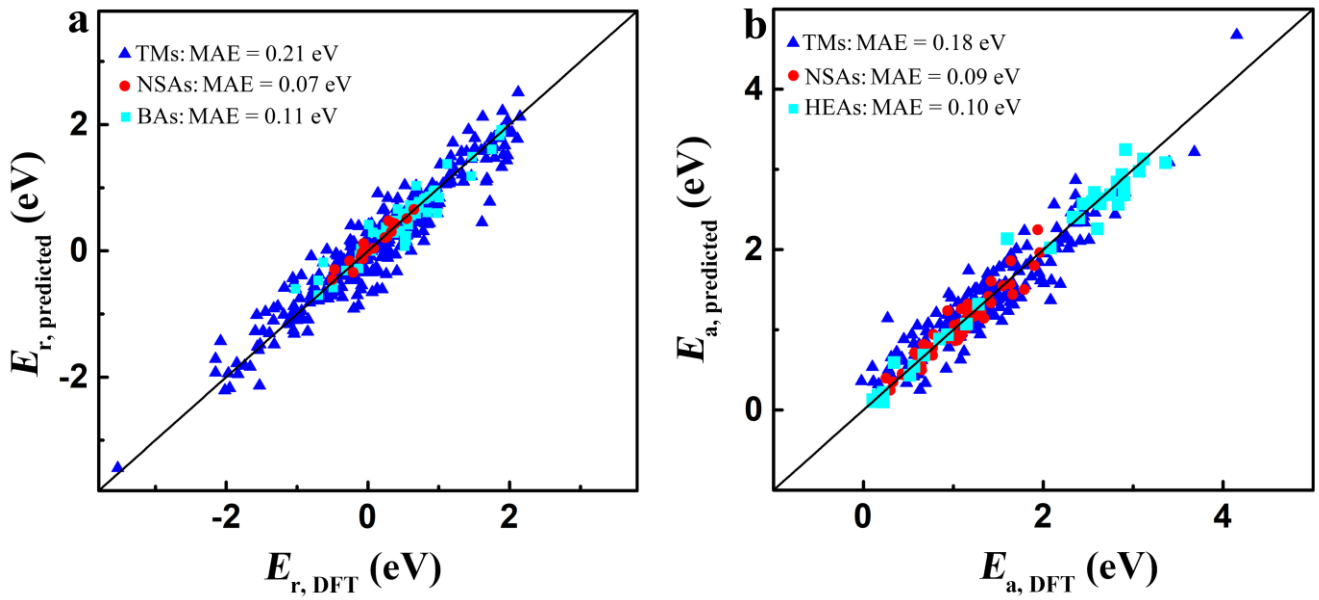

Figure S42. Comparison between the predicted reaction energies (E_r) and activation energies (E_a) and the DFT-calculated ones on TMs, NSAs, BAs and HEAs[13,14,18-29].

Table S1. Comparison between the predicted prefactors μ_1 and μ_2 of D_{ad} and $\overline{CN}$ terms of Eq. (3) in the main text and the DFT-calculated ones for the different adsorbates at the top site of TMs[11], and of NSAs, BAs, and HEAs in the adsorption-site effect of alloying. Columns 2 and 3 show the values of X_m and X of the corresponding adsorbate, Columns 4 and 5 show the predicted values of μ_1 and μ_2, while Columns 6-13 show the fitted ones that corresponding to Fig. 2a-e in the main text and Fig. S13b.

Species	X_m	X	Predicted		DFT-calculated							
					TMs		NSAs		BAs		HEAs	
			μ_1	μ_2	μ_1	μ_2	μ_1	μ_2	μ_1	μ_2	μ_1	μ_2
CH	4	1	0.060	0.080	0.062	0.081					0.054	0.080
CH_2	4	2	0.040	0.120	0.040	0.111	0.035	0.099	0.040	0.120	0.035	0.125
CH_3	4	3	0.020	0.160	0.016	0.117					0.015	0.120
CO	4	2	0.040	0.120	0.033	0.114					0.033	0.122
CCH_3	4	1	0.060	0.080	0.064	0.079						
NH	3	1	0.050	0.100	0.047	0.105					0.038	0.098
NH_2	3	2	0.025	0.150	0.024	0.148	0.021	0.141	0.026	0.105	0.025	0.145
OH	2	1	0.033	0.134	0.021	0.156	0.018	0.138	0.023	0.168	0.022	0.135

Table S2. Comparison between the predicted prefactors μ_1 and μ_2 of D_{ad} and $\overline{CN}$ terms of Eq. (3) in the main text and the DFT-calculated ones for the different adsorbates at the various adsorption sites of TMs[12]. Columns 2 and 3 show the predicted values while Columns 4-11 show the fitted ones that corresponding to Fig. S13c-f. Note that the horizontal line for the prefactor μ_2 denotes that the corresponding available data are obtained based on the variation of the electronic structures instead of the geometric structures.

Species	**Predicted**		**TMs**							
			(100)		**(111)**		**(211)**			
			four-fold		hcp		hcp		four-fold	
	μ_1	μ_2	μ_1	μ_2	μ_1	μ_2	μ_1	μ_2	μ_1	μ_2
CH	0.060	0.080	0.062	——	0.068	——	0.063	0.082	0.058	——
Species	**Predicted**		**(100)**		**(110)**		**(211)**			
			bridge		top		top		bridge	
	μ_1	μ_2	μ_1	μ_2	μ_1	μ_2	μ_1	μ_2	μ_1	μ_2
CO	0.040	0.120	0.037	——	0.033	——	0.033	0.117	0.038	0.114

Table S3. The coefficients k_1 and k_2 of Eq. (5) in the main text for the adsorption energy on NSAs, BAs, and HEAs in the adsorption-site and environmental effects of alloying. Rows 1 and 2 correspond to the adsorption energy of CH_x (x = 1-3), CO, NH_x (x = 1, 2), and OH on CuM NSAs, AgM BAs, and RuRhIrPdPt-based HEAs in the adsorption-site effect of alloying (Fig. 2c-e in the main text and Figs. S14b, S20 and S21). Rows 3-14 correspond to the adsorption energy of CH_x (x = 0-3), CO, NH_x (x = 0-2), OH, F, and Cl on Pt(Pd)M NSAs[9,15–17], CH_2 on AgM BAs, and CH_2 and CO on Ru(Cu)RhIrPdPt HEAs in the environmental effect of alloying (Fig. 2c and d in the main text and Fig. S22), while Rows 15-20 correspond to the adsorption energy of OH, H, and OH+H on CuNi NSAs[13,14], C, CH and CO on AgAu, AgPd, IrRu, PtRh BAs[12], OH on Ag_3M BAs[18], and OH on RuRhIrPdPt HEAs in both the adsorption-site and environmental effects of alloying (Fig. 2f in the main text and Figs. S23 and S24).

Adsorption-site effect on NSAs, BAs, and HEAs	**All considered adsorbates**	k_1	k_2								
		0.10	0.90								
Environmental effect	**NSAs**	**PtM**		**PtM**		**PtM**		**PtM**		**PdM**	
		CH_x (x = 0-3) and NH_x (x = 0-2)		CO		OH		F and Cl		CO	
		k_1	k_2	k_1	k_2	k_1	k_2	k_1	k_2	k_1	k_2
		-0.65	1.00	-0.50	1.00	-1.36	1.00	-1.00	1.00	-0.36	1.00
	CH_2 on BAs	k_1	k_2								
		-0.08	1.22								
	CH_2 on HEAs	**Ru**		**Rh**		**Ir**		**Pd**		**Pt**	
		k_1	k_2	k_1	k_2	k_1	k_2	k_1	k_2	k_1	k_2
		0.54	0.80	1.22	0.10	3.68	-4.60	2.12	-0.80	0.45	0.50
	CO on HEAs	**Ru**		**Cu**							
		k_1	k_2	k_1	k_2						
		2.08	-0.35	0.01	1.00						
Adsorption-site and environmental effects	**OH, H, and OH+H on NSAs**	k_1	k_2								
		0.28	0.34								
	C, CH, CO and OH on BAs	k_1	k_2								
		1.00	0.10								
	OH on HEAs	k_1	k_2								
		0.90	-0.10								

Table S4. Comparison between the predicted prefactors μ_1 and μ_2 of D_{ad} and $\overline{CN}$ terms of Eq. (3) in the main text and the DFT-calculated ones for CH_x (x = 0-3), CO, NH_x (x = 0-2), OH, F, and Cl at the top site of (111) and (100) surfaces of Pt(Pd)M NSAs[9,15–17] in the environmental effect of alloying, and for OH at the fcc sites of (111) surface of CuNi NSAs with the different Cu/Ni ratios[13,14] in both the adsorption-site and environmental effects of alloying. Columns 2 and 3 show the predicted values while Columns 4-11 show the fitted ones that corresponding to Figs. S22 and S24b-e. Note that the horizontal line for the prefactor μ_2 denotes that the corresponding available data are obtained based on the variation of the electronic structures instead of the geometric structures.

Species	**Predicted**		**Environmental effect of alloying**							
			i[15]		**ii**[16]		**iii**[9]		**iv**[17]	
	μ_1	μ_2	μ_1	μ_2	μ_1	μ_2	μ_1	μ_2	μ_1	μ_2
C	0.080	0.040	0.086	——						
CH	0.060	0.080	0.085	——						
CH_2	0.040	0.120	0.038	——						
CH_3	0.020	0.160	0.028	——						
CO	0.040	0.120	0.044	——	0.035/0.040	——				
N	0.075	0.050	0.076	——						
NH	0.050	0.100	0.066	——						
NH_2	0.025	0.150	0.023	——						
OH	0.033	0.134					0.033	——		
F	0.050	0.100							0.055	——
Cl	0.050	0.100							0.049	——
Species	**Predicted**		**Adsorption-site and environmental effects of alloying**							
			i[13]		**ii**[14]		**iii**[14]			
			Cu-based		**Cu-based**		**Ni-based**			
	μ_1	μ_2	μ_1	μ_2	μ_1	μ_2	μ_1	μ_2		
OH	0.033	0.134	0.033	——	0.032	——	0.034	——		

Table S5. Comparison between the predicted prefactors μ_1 and μ_2 of D_{ad} and $\overline{CN}$ terms of Eq. (3) in the main text and the DFT-calculated ones for C, CH, and CO at the bridge, fcc, hcp and four-fold sites of (211) surface of AgAu, AgPd, IrRu, and PtRh BAs[12] in both the adsorption-site and environmental effects of alloying, and for OH at the hcp sites of (111) surface of Ag_3M BAs[18] in both the adsorption-site and environmental effects of alloying. Columns 2 and 3 show the predicted values while Columns 4-11 show the fitted ones that corresponding to Fig. 2f in the main text and Figs. S23 and S24a. Note that the horizontal line for the prefactor μ_2 denotes that the corresponding available data are obtained based on the variation of the electronic structures instead of the geometric structures.

Species	**Predicted**		**BAs**							
			bridge		**fcc**		**hcp**		**four-fold**	
	μ_1	μ_2	μ_1	μ_2	μ_1	μ_2	μ_1	μ_2		
C	0.080	0.040					0.064	0.041	0.065	0.042
CH	0.060	0.080	0.066	———	0.051	0.072	0.056	0.079	0.054	0.076
CO	0.040	0.120	0.034	0.119						
OH	0.033	0.134					0.026	———		

Table S6. The accuracy comparison of Eqs. (3-5) in the main text in predicting the adsorption energy on TMs, NSAs, BAs, and HEAs in the adsorption-site effect of alloying in dissolution, by introducing the cohesive energy and the *d*-band width of the adsorption sites' TM atoms.

	MAE (eV)	
	Cohesive energy	***d*-band width**
TMs	0.16	0.32
NSAs	0.23	0.34
BAs	0.14	0.38
HEAs	0.19	0.41

Table S7. Comparison between the predicted prefactors λ_{r1} and λ_{r2} of the D_{ad} and $\overline{CN}$ terms of Eqs. (S5) and (S6) and the DFT-calculated ones for reaction energies of electrochemical and thermochemical reactions on TMs, NSAs, and BAs. Columns 3 and 4 show the predicted values while Columns 5-12 show the fitted ones in Figs. S27-S29 and S34. The superscripts i-v denote the Ref. [21], Ref. [25], Ref. [23], Ref. [18] and Ref. [24]. The superscripts a and b denote the reaction energy on Cu- and Ni-based NSAs, c and d denote the reaction energy at the hcp and top sites, while e and f do the reaction energy on AgM and CoM BAs. Note that the horizontal line for the prefactor λ_{r2} denotes that the corresponding available data are obtained based on the variation of the electronic structures instead of the geometric structures.

Electrochemical reactions											
	Reactions	**Predicted**		**DFT-fitted**							
				Ref. [20]							
		λ_{r1}	λ_{r2}	λ_{r1}	λ_{r2}						
TMs	$CO_2+H^++e^- \rightarrow COOH^*$	0.027	0.054	0.024	—						
	$COOH^*+H^++e^- \rightarrow CO^*+H_2O$	0.013	0.026	0.017	—						
	$CO^*+H^++e^- \rightarrow COH^*$	0.027	0.054	0.029	—						
	$CO^*+H^++e^- \rightarrow CHO^*$	0.010	0.020	0.007	—						
	$COH^*+H^++e^- \rightarrow C^*+H_2O$	0.013	0.026	0.016	—						
	$C^*+H^++e^- \rightarrow CH^*$	0.020	0.040	0.017	—						
	$CH^*+H^++e^- \rightarrow CH_2^*$	0.020	0.040	0.026	—						
	$CH_2^*+H^++e^- \rightarrow CH_3^*$	0.020	0.040	0.021	—						
	$CH_3^*+H^++e^- \rightarrow CH_4$	0.020	0.040	0.019	—						
	$COH^*+H^++e^- \rightarrow CHOH^*$	0.020	0.040	0.022	—						
	$CHOH^*+H^++e^- \rightarrow CH_2OH^*$	0.020	0.040	0.020	—						
	$CH_2OH^*+H^++e^- \rightarrow CH_3OH$	0.020	0.040	0.022	—						
Thermochemical reactions											
	Reactions	**Predicted**		**DFT-fitted**							
								Ref. [19]		Ref. [22]	
		λ_{r1}	λ_{r2}	λ_{r1}	λ_{r2}	λ_{r1}	λ_{r2}	λ_{r1}	λ_{r2}	λ_{r1}	λ_{r2}
TMs	$CH_4 \rightarrow CH_3^* + H^*$	0.030	0.060	0.030[i]	—	0.042[iv]	0.060[iv]			0.039	0.060
	$CH_3^* \rightarrow CH_2^* + H^*$	0.030	0.060	0.031[ii]	0.059[ii]	0.038[v]	0.060[v]			0.038	0.060
	$CH_2^* \rightarrow CH^* + H^*$	0.030	0.060	0.036[ii]	0.059[ii]	0.043[v]	0.060[v]				
	$CH^* \rightarrow C^* + H^*$	0.030	0.060	0.030[ii]	0.060[ii]						
	$NH_3^* \rightarrow NH_2^* + H^*$	0.038	0.075	0.033[iii]	0.089[iii]			0.044	0.480		
	$NH_2^* \rightarrow NH^* + H^*$	0.038	0.075	0.037[iii]	0.096[iii]			0.032	0.081		
	$NH^* \rightarrow N^* + H^*$	0.038	0.075	0.038[iii]	0.076[iii]						
	$N_2 \rightarrow 2N^*$	0.113	0.225	0.118[iii]	0.213[iii]						
	$OH^* \rightarrow O^* + H^*$	0.050	0.100			0.049[iv]	0.098[iv]	0.041	0.103		
NSAs	**Reactions**	**Predicted**		**DFT-fitted**							
				Ref. [13]		Ref. [14]		Ref. [14]			
		λ_{r1}	λ_{r2}	λ_{r1}	λ_{r2}	λ_{r1}	λ_{r2}	λ_{r1}	λ_{r2}		
	$OH^* + H^* \rightarrow H_2O$	0.050	0.100	0.043	—						
	$H_2O \rightarrow OH^* + H^*$	0.050	0.100			0.052[a]	—	0.049[b]	—		
BAs	**Reactions**	**Predicted**		**DFT-fitted**							
				Ref. [18]		Ref. [18]					
		λ_{r1}	λ_{r2}	λ_{r1}	λ_{r2}	λ_{r1}	λ_{r2}				
	$CH_4 \rightarrow CH_3^* + H^*$	0.030	0.060	0.033[c]	—	0.024[d]	—				
	$CH_3^* \rightarrow CH_2^* + H^*$	0.030	0.060	0.026[e]	0.059[e]	0.031[f]	0.059[f]				
	$CH_2^* \rightarrow CH^* + H^*$	0.030	0.060	0.034	0.061						
	$CH^* \rightarrow C^* + H^*$	0.030	0.060	0.025	0.062						
	$NH^* \rightarrow N^* + H^*$	0.038	0.075	0.046	0.074						

Table S8. Comparison between the predicted prefactors λ_{a1} and λ_{a2} of the D_{ad} and $\overline{CN}$ terms of Eqs. (S7) and (S8) and the DFT-calculated ones for activation energies of electrochemical and thermochemical reactions on TMs and NSAs. Columns 3 and 4 show the predicted values while Columns 5-14 show the fitted ones that corresponding to Figs. S31, S32, and S35. The superscripts i and ii denote the Ref. [22] and Ref. [23] respectively, while the superscripts a and b denote the activation energy on Cu- and Ni-based NSAs. Note that the horizontal line for the prefactor λ_{a2} denotes that the corresponding available data are obtained based on the variation of the electronic structures instead of the geometric structures.

Electrochemical reactions													
TMs	**Reactions**	**Predicted**		**DFT-fitted**									
				Ref. [27]									
		λ_{a1}	λ_{a2}	λ_{a1}	λ_{a2}								
	$CO^{*}+H^{+}+e^{-} \rightarrow CHO^{*}$	0.009	0.017	0.015	0.018								
Thermochemical reactions													
TMs	**Reactions**	**Predicted**		**DFT-fitted**									
						Ref. [19]		Ref. [29]		Ref. [21]		Ref. [24]	
		λ_{a1}	λ_{a2}	λ_{a1}	λ_{a2}	λ_{a1}	λ_{a2}	λ_{a1}	λ_{a2}	λ_{a1}	λ_{a2}	λ_{a1}	λ_{a2}
	$CH_4 \rightarrow CH_3^{*} + H^{*}$	0.026	0.051	0.029[i]	0.051[i]			0.037	—	0.029	—		
	$CH_3^{*} \rightarrow CH_2^{*} + H^{*}$	0.026	0.051	0.030[i]	0.051[i]			0.035	—			0.038	0.051
	$CH_2^{*} \rightarrow CH^{*} + H^{*}$	0.026	0.051					0.037	—			0.036	0.051
	$CH^{*} \rightarrow C^{*} + H^{*}$	0.026	0.051					0.029	—				
	$NH_3^{*} \rightarrow NH_2^{*} + H^{*}$	0.027	0.054	0.019[ii]	0.054[ii]	0.030	0.047						
	$NH_2^{*} \rightarrow NH^{*} + H^{*}$	0.027	0.054	0.029[ii]	0.060[ii]	0.025	0.203						
	$NH^{*} \rightarrow N^{*} + H^{*}$	0.027	0.054	0.027[ii]	0.050[ii]								
	$N_2 \rightarrow 2N^{*}$	0.080	0.161	0.081[ii]	0.154[ii]								
	$OH^{*} \rightarrow O^{*} + H^{*}$	0.029	0.057			0.027	0.056						
NSAs	**Reactions**	**Predicted**		**DFT-fitted**									
				Ref. [28]		Ref. [13]		Ref. [14]		Ref. [14]		Ref. [26]	
		λ_{a1}	λ_{a2}	λ_{a1}	λ_{a2}	λ_{a1}	λ_{a2}	λ_{a1}	λ_{a2}	λ_{a1}	λ_{a2}	λ_{a1}	λ_{a2}
	$CH_4 \rightarrow CH_3^{*} + H^{*}$	0.026	0.051	0.021	—								
	$CH_3^{*} \rightarrow CH_2^{*} + H^{*}$	0.026	0.051	0.028	—								
	$CH_2^{*} \rightarrow CH^{*} + H^{*}$	0.026	0.051	0.027	—								
	$CH^{*} \rightarrow C^{*} + H^{*}$	0.026	0.051	0.017	—								
	$OH^{*} + H^{*} \rightarrow H_2O$	0.029	0.057			0.028	—						
	$H_2O \rightarrow OH^{*} + H^{*}$	0.029	0.057					0.035[a]	—	0.027[b]	—		
	$2H^{*} \rightarrow H_2$	0.032	0.064									0.036	—

References

1 W. Gao, Y. Chen, B. Li, S.-P. Liu, X. Liu and Q. Jiang, *Nat. Commun.*, 2020, **11**, 1196.

2 J. K. Nørskov and N. D. Lang, *Phys. Rev. B*, 1980, **21**, 2131–2136.

3 F. Abild-Pedersen, J. Greeley, F. Studt, J. Rossmeisl, T. R. Munter, P. G. Moses, E. Skúlason, T. Bligaard and J. K. Nørskov, *Phys. Rev. Lett.*, 2007, **99**, 016105.

4 M. A. Turchanin and P. G. Agraval, *Powder Metall. Met. Ceram.*, 2008, **47**, 26–39.

5 A. Pasturel, C. Colinet and P. Hicter, *Acta Metall.*, 1984, **32**, 1061–1067.

6 D. G. Pettifor, *Solid State Commun.*, 1978, **28**, 621–623.

7 M. Cyrot and F. Cyrot-Lackmann, *J. Phys. F Met. Phys.*, 1976, **6**, 2257–2265.

8 W. A. Harrison, *Electronic structure and the properties of solids*, Freeman, New York, 1980.

9 H. Xin, A. Holewinski and S. Linic, *ACS Catal.*, 2012, **2**, 12–16.

10 M. J. Hoffmann, A. J. Medford and T. Bligaard, *J. Phys. Chem. C*, 2016, **120**, 13087–13094.

11 L. T. Roling and F. Abild-Pedersen, *ChemCatChem*, 2018, **10**, 1643–1650.

12 M. Andersen, S. V. Levchenko, M. Scheffler and K. Reuter, *ACS Catal.*, 2019, **9**, 2752–2759.

13 L.-Y. Gan, R.-Y. Tian, X.-B. Yang, H.-D. Lu and Y.-J. Zhao, *J. Phys. Chem. C*, 2012, **116**, 745–752.

14 S. Ghosh, S. Hariharan and A. K. Tiwari, *J. Phys. Chem. C*, 2017, **121**, 16351–16365.

15 H. Xin, A. Holewinski, N. Schweitzer, E. Nikolla and S. Linic, *Top. Catal.*, 2012, **55**, 376–390.

16 X. Ma, Z. Li, L. E. K. Achenie and H. Xin, *J. Phys. Chem. Lett.*, 2015, **6**, 3528–3533.

17 F. Calle-Vallejo, J. I. Martínez, J. M. García-Lastra, J. Rossmeisl and M. T. M. Koper, *Phys. Rev. Lett.*, 2012, **108**, 116103.

18 O. Mamun, K. T. Winther, J. R. Boes and T. Bligaard, *Sci. Data*, 2019, **6**, 76.

19 S. Wang, B. Temel, J. Shen, G. Jones, L. C. Grabow, F. Studt, T. Bligaard, F. Abild-Pedersen, C. H. Christensen and J. K. Nørskov, *Catal. Letters*, 2011, **141**, 370–373.

20 C. Shi, H. A. Hansen, A. C. Lausche and J. K. Nørskov, *Phys. Chem. Chem. Phys.*, 2014, **16**, 4720.

21 D. Hibbitts and M. Neurock, *Surf. Sci.*, 2016, **650**, 210–220.

22 B. Xing, X.-Y. Pang and G.-C. Wang, *J. Catal.*, 2011, **282**, 74–82.

23 T. Wang and F. Abild-Pedersen, *Proc. Natl. Acad. Sci.*, 2021, **118**, e2106527118.

24 J. Schumann, A. J. Medford, J. S. Yoo, Z.-J. Zhao, P. Bothra, A. Cao, F. Studt, F. Abild-Pedersen and J. K. Nørskov, *ACS Catal.*, 2018, **8**, 3447–3453.

25 M. H. Hansen, J. K. Nørskov and T. Bligaard, *J. Catal.*, 2019, **374**, 161–170.

26 E. J. Evans, H. Li, W. Y. Yu, G. M. Mullen, G. Henkelman and C. B. Mullins, *Phys. Chem. Chem. Phys.*, 2017, **19**, 30578–30589.

27 X. Liu, J. Xiao, H. Peng, X. Hong, K. Chan and J. K. Nørskov, *Nat. Commun.*, 2017, **8**, 15438.

28 C. Fan, Y. A. Zhu, Y. Xu, Y. Zhou, X. G. Zhou and D. Chen, *J. Chem. Phys.*, 2012, **137**, 014703.

29 Y. Wang, L. Xiao, Y. Qi, M. Mahmoodinia, X. Feng, J. Yang, Y.-A. Zhu and D. Chen, *Phys. Chem. Chem. Phys.*, 2019, **21**, 19269–19280.

30 S. Trasatti, *J. Electroanal. Chem. Interfacial Electrochem.*, 1972, **39**, 163–184.

31 S. Wu, Y. Pan, J. Lu, N. Wang, W. Dai and T. Lu, *J. Mater. Sci. Technol.*, 2019, **35**, 1629–1635.

32 H.-J. Qiu, G. Fang, J. Gao, Y. Wen, J. Lv, H. Li, G. Xie, X. Liu and S. Sun, *ACS Mater. Lett.*, 2019, **1**, 526–533.

33 P. Xie, Y. Yao, Z. Huang, Z. Liu, J. Zhang, T. Li, G. Wang, R. Shahbazian-Yassar, L. Hu and C. Wang, *Nat. Commun.*, 2019, **10**, 4011.

34 T. Löffler, H. Meyer, A. Savan, P. Wilde, A. Garzón Manjón, Y.-T. Chen, E. Ventosa, C. Scheu, A. Ludwig and W. Schuhmann, *Adv. Energy Mater.*, 2018, **8**, 1802269.

35 E. L. Clark, C. Hahn, T. F. Jaramillo and A. T. Bell, *J. Am. Chem. Soc.*, 2017, **139**, 15848–15857.

36 V. Tripkovic, H. A. Hansen, J. Rossmeisl and T. Vegge, *Phys. Chem. Chem. Phys.*, 2015, **17**, 11647–11657.

37 K. P. Kuhl, T. Hatsukade, E. R. Cave, D. N. Abram, J. Kibsgaard and T. F. Jaramillo, *J. Am. Chem. Soc.*, 2014, **136**, 14107–14113.

38 J. K. Nørskov, T. Bligaard, A. Logadottir, J. R. Kitchin, J. G. Chen, S. Pandelov and U. Stimming, *J. Electrochem. Soc.*, 2005, **152**, J23.

39 M. Escudero-Escribano, P. Malacrida, M. H. Hansen, U. G. Vej-Hansen, A. Velazquez-Palenzuela, V. Tripkovic, J. Schiotz, J. Rossmeisl, I. E. L. Stephens and I. Chorkendorff, *Science*, 2016, **352**, 73–76.

40 T. Bligaard, J. K. Nørskov, S. Dahl, J. Matthiesen, C. H. Christensen and J. Sehested, *J. Catal.*, 2004, **224**, 206–217.

41 J. K. Pedersen, T. A. A. Batchelor, D. Yan, L. E. J. Skjegstad and J. Rossmeisl, *Curr. Opin. Electrochem.*, 2021, **26**, 100651.

42 J. P. Perdew, K. Burke and M. Ernzerhof, *Phys. Rev. Lett.*, 1996, **77**, 3865–3868.

43 B. Hammer, L. B. Hansen and J. K. Nørskov, *Phys. Rev. B*, 1999, **59**, 7413–7421.

44 J. P. Perdew, J. A. Chevary, S. H. Vosko, K. A. Jackson, M. R. Pederson, D. J. Singh and C. Fiolhais, *Phys. Rev. B*, 1992, **46**, 6671–6687.

45 G. Zhang, *Understanding the Role of van Der Waals Forces in Solids from First Principles*. Freie Universität Berlin, 2014.

46 J. Wellendorff, K. T. Lundgaard, A. Møgelhøj, V. Petzold, D. D. Landis, J. K. Nørskov, T. Bligaard and K. W. Jacobsen, *Phys. Rev. B*, 2012, **85**, 235149.

47 X. Guan, C. Zhao, X. Liu, S. Liu, W. Gao and Q. Jiang, *J. Phys. Chem. C*, 2020, **124**, 25898–25906.

48 L. Qi, W. Gao and Q. Jiang, *J. Phys. Chem. C*, 2020, **124**, 23134–23142.

49 S. Grimme, J. Antony, S. Ehrlich and H. Krieg, *J. Chem. Phys.*, 2010, **132**, 154104.